Flow (2026), **6** E17
doi:10.1017/flo.2026.10055

FLOW CAMBRIDGE UNIVERSITY PRESS

RESEARCH ARTICLE

Biglobal input–output analysis of separated flow over a periodic hill

Jino George and Chang Liu

School of Mechanical, Aerospace and Manufacturing Engineering, University of Connecticut, Storrs, CT, USA
Corresponding author: Chang Liu; Email: chang_liu@uconn.edu

Received: 22 January 2026 UTC; **Revised:** 6 May 2026 UTC; **Accepted:** 18 May 2026 UTC

Keywords: flow separation; flow over a periodic hill; input–output analysis

Abstract

This paper performs a biglobal input–output analysis of the separated flow over a periodic hill to understand the flow sensitivity to disturbances. We use the volume penalty method to model the solid body of the periodic hill, which is implemented in a spectral solver to obtain the two-dimensional base flow used in the biglobal input–output analysis. We formulate the spatiotemporal frequency response operator using the tensor product, and conduct singular value decomposition of this frequency response operator to identify the dominant response mode, forcing mode and input–output amplification. Results show that disturbances with high temporal frequencies result in shear-dominant flow structures with a smaller length scale, while as the temporal frequency approaches zero, the response modes are less oscillatory in the spatial domain and display global recirculation. With an increase in the spanwise wavenumber of disturbances, flow structures grow in length scale and become less oscillatory in space, while the amplification increases and then decreases with increasing spanwise wavenumber. In general, forcing modes show a peak near the separation region downstream of the hill crest, while the response modes show a peak near the reattachment region upstream of the hill crest.

Impact statement

This work performs a biglobal input–output analysis of a canonical separated flow over a periodic hill. Results provide insights into the flow sensitivity, identifying the region and spatiotemporal scales where the external disturbance will be most effective in manipulating the flow response. Our input–output analysis also identifies the corresponding flow response and input–output amplification under the most sensitive disturbance. These insights can inform the flow sensitivity, receptivity, transition to turbulence and flow control of separated flows in engineering and geophysical applications, such as the flow over mountainous terrain, flow over an aerofoil and flow over blade tips in a turbine. Moreover, our biglobal input–output analysis employs the tensor product to directly construct differentiation matrices and associated spatiotemporal frequency response operator over a tensor product grid, which allows more flexibility to generalise this framework to a wider class of separated flows over complex geometries.

1. Introduction

Fluid flow over complex and curved structures is a very common scenario in engineering problems and in nature. These physical problems manifest themselves in real-world applications, such as in turbomachinery, aerospace engineering and geophysical applications (Almeida *et al*. 1993). Some of these examples include flow over guiding vanes or blade tips in a turbine (Wheeler & Sandberg 2016), flow over an

© The Author(s), 2026. Published by Cambridge University Press. This is an Open Access article, distributed under the terms of the Creative Commons Attribution licence (https://creativecommons.org/licenses/by/4.0/), which permits unrestricted re-use, distribution and reproduction, provided the original article is properly cited.

https://doi.org/10.1017/flo.2026.10055 Published online by Cambridge University Press

aerofoil (Rolandi *et al*. 2025) or more naturally occurring flow over mountains (Belcher & Hunt 1998). An important feature of these flows is the flow separation, which can be characterised by wall-layer thickening and recirculation with an increase in the wall-normal velocity field. Flow over a periodic hill is a canonical benchmark for understanding separated flows (Almeida *et al*. 1993; Breuer *et al*. 2009; Günther & Von Rohr 2003; Li *et al*. 2025; Rapp & Manhart 2011; Xiao *et al*. 2020; Zhou *et al*. 2023), and it has been experimentally and numerically studied extensively. For example, Almeida *et al*. (1993) studied and measured mean and fluctuating flow over a periodic hill in both streamwise and spanwise directions. Various numerical and experimental studies were conducted to investigate flow separation, recirculation and reattachment (Breuer *et al*. 2009; Günther & Von Rohr 2003; Rapp & Manhart 2011). Direct numerical simulations (DNS) of a series of flows over periodic hills were also compiled as a database for data-driven turbulence modelling (Xiao *et al*. 2020).

Understanding and predicting flow separation over complex structures can be a difficult process because flow separation over curved surfaces is sensitive to various factors, such as incoming flow disturbance, the geometry of the structure, streamwise pressure gradient and interaction with the outer flow regime (Breuer *et al*. 2009; Rapp & Manhart 2011). Another example of sensitivity to disturbances in separated flow is provided by Rolandi *et al*. (2025), where the transition from wake-dominated structures to shear-dominated structures is observed as the disturbance frequency increases. Here, shear-dominated structures are flow structures with shorter length scales, which are more energetic and localised near the separation point and typically have higher temporal frequencies close to the characteristic frequency of a free shear layer (Ho and Huerre 1984; Kotapati *et al*. 2010; Rolandi *et al*. 2025). This shear-dominated dynamics is in contrast to that of global wake-dominated structures, which are less oscillatory and more coherent in space, seen at lower temporal frequencies of disturbances.

Uncovering the dominant flow structures that are generated and evolved by separated flow is important for solving the real-world problems we mentioned above. Modal analysis or decomposition has been utilised to extract the dominant flow structures while reducing the model complexity of the flow (Kutz *et al*. 2016; Schmid & Henningson 2012; Taira *et al*. 2017; Theofilis 2011). These techniques help in the modelling, analysis and control of the fluid-flow system, thereby helping in achieving model-based design of various systems (Bagheri *et al*. 2009; Brunton and Noack 2015; Jovanović 2021; Luhar *et al*. 2015; Moarref & Jovanović 2012; Ran *et al*. 2021; Rowley & Dawson 2017). Modal analysis techniques can be classified into data-driven or operator-based approaches (Rolandi *et al*. 2024; Taira *et al*. 2017, 2020). Data-driven methods, such as dynamic mode decomposition, have been used to find a lower-order subspace to capture the effects of wake behind a flexible membrane and a jet passing between two cylinders (Schmid 2010). Recently, information-theoretic machine learning has also been used for mode decomposition of separated flows over an aerofoil (Fukami & Araki 2026).

Physics- or operator-based modal analysis includes global linear stability analysis (Jouin *et al*. 2024; Taira *et al*. 2020; Tatsumi & Yoshimura 1990; Theofilis 2011; Yu *et al*. 2016) and input–output or resolvent analysis (Bamieh & Dahleh 2001; Farrell & Ioannou 1993; Jovanović & Bamieh 2005; Jovanović 2021; Liu & Gayme 2020, 2021; McKeon 2017). Both methods rely on the linearised Navier–Stokes equations and depend on the base flow obtained from DNS or experimental results for identifying the dominant flow structures. To conduct global linear stability analysis, we need to construct a linear operator from linearised Navier–Stokes equations and then perform an eigenvalue analysis of this linear operator to obtain the growth rate (Moradi & Floryan 2014; Picella *et al*. 2018; Sun *et al*. 2017; Szumbarski & Floryan 2006; Theofilis 2011; de Vicente *et al*. 2014). Input–output or resolvent analysis considers the linearised Navier–Stokes equation disturbed by an additional forcing term, which can represent free-stream disturbance, experimental uncertainty, background noise and model uncertainty. Such input forcing is then mapped to certain outputs of interest through a spatiotemporal frequency response operator or a resolvent operator. At every wavenumber–frequency combination, the singular value decomposition of the frequency response operator is performed (Jovanović, 2021; McKeon 2017; Rolandi *et al*., 2024), which uncovers the dominant or most amplified flow structures. Such singular value decomposition also identifies how minimal forcing can cause an exaggerated response at certain

https://doi.org/10.1017/flo.2026.10055 Published online by Cambridge University Press

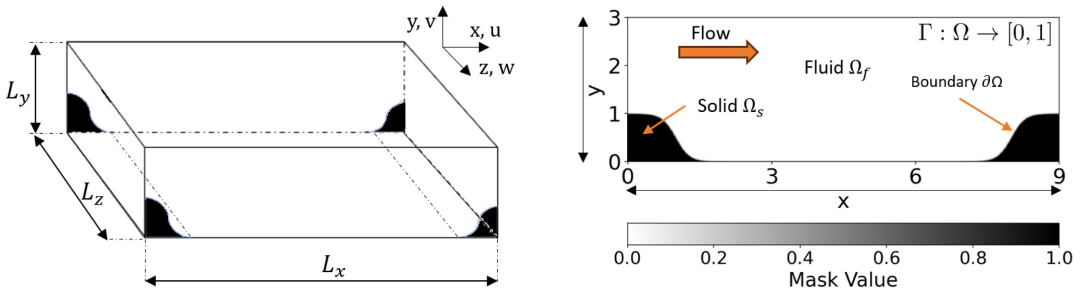
frequencies, which makes it an effective tool for guiding active flow control (Lin *et al*. 2023; Liu *et al*. 2021; Yeh & Taira 2019).

Resolvent analysis has also been extended to analyse flow over complex geometry, such as riblets (Chavarin & Luhar 2020; Ran *et al*. 2021; Naseri & Zare 2025), compliant walls (Luhar *et al*. 2015) and porous substrates (Chavarin *et al*. 2021). For flow over riblets, resolvent analysis can help design and optimise the geometry of riblets, allowing us to understand the dynamics of secondary flow generated under various protrusion heights of the ribs (Chavarin & Luhar 2020). Furthermore, such resolvent analysis has been exploited to understand flow separation and reattachment at various frequencies of separated flow over an aerofoil (Houtman *et al*. 2023; Ribeiro & Taira 2024; Rolandi *et al*. 2025; Thomareis & Papadakis 2018; Yeh *et al*. 2020). Moreover, resolvent analysis of cavity flow shows that forcing mode peaks near the leading edge of the cavity, while response mode peaks at certain downstream locations close to the trailing edge (Islam & Sun 2024; Liu & Gaitonde 2021; Sun *et al*. 2020). By understanding the least stabilising frequencies through resolvent analysis, increased aerodynamic loading can be achieved by laminar separation control (Gross *et al*. 2024). Understanding flow separation, recirculation and reattachment through input–output analysis can be extended to other separated flows or wake flows, such as flow over cylinders and other stationary or moving objects (Feng *et al*. 2024; Jin *et al*. 2021; Li & Yang 2024; Lin *et al*. 2023).

Within resolvent analysis, a complex geometry is usually modelled as the volume penalty method (VPM) (Chavarin & Luhar 2020; Ran *et al*. 2021). The VPM uses a Brinkman-type penalisation with varying permeability to model a solid system immersed within a fluid domain (Angot 1999), in the same spirit as the immersed boundary method (Mittal & Iaccarino 2005; Peskin 2002; Taira & Colonius 2007; Verzicco 2023). These methods allow us to couple the fluid and the solid system in a single numerical domain (Angot 1999), and thus avoid the body-fitting grid and coordinate transformation required in classical methods such as the arbitrary Lagrangian–Eulerian method (Diosady & Murman 2014). The VPM approximates the no-slip boundary condition by rapid linear damping (Hester *et al*. 2021) and can be extended to moving and deformable bodies (Engels *et al*. 2015). Although some recent work implements the immersed boundary method within resolvent analysis (Flynn *et al*. 2024; Hou & Colonius 2023), the VPM has an advantage in that it does not require computing the penalty body force through interpolation, which is more suitable for resolvent or input–output analysis performed in the frequency domain (Chavarin & Luhar 2020; Ran *et al*. 2021).

In this work, we conduct a biglobal input–output analysis of flow over a periodic hill to uncover the underlying dominant flow structures and to understand the flow sensitivity to disturbance. The streamwise periodicity of this flow allows us to isolate the flow separation from the spatially developing effects, and the smooth geometry of the periodic hill also allows us to avoid the Rossiter modes (Rossiter 1964; Sun *et al*. 2017) observed in flow over a rectangular cavity. We model the periodic hill using an improved VPM framework, where asymptotic analysis has been conducted to determine an optimal mask function that can lead to improved accuracy (Hester *et al*. 2021). This improved VPM approach has a faster convergence rate of the model error as the damping time scale approaches zero (Hester *et al*. 2021), compared with previous VPM frameworks (Angot 1999; Carbou & Fabrie 2003). We utilise the same VPM model in both DNS and input–output analysis. We use DNS to generate the two-dimensional (2-D) base flows, which are then used to formulate the resolvent operator within biglobal input–output analysis. Here, biglobal is used in the same sense as in biglobal linear stability analysis (Theofilis 2011), where our base flow depends on two spatial coordinates: streamwise and wall-normal directions. Similar biglobal resolvent or input–output analysis has been widely employed to 2-D base flow induced by streamwise-travelling waves (Moarref & Jovanović 2010), flow over riblets (Chavarin & Luhar 2020; Ran *et al*. 2021) and separated flow over an aerofoil (Ribeiro & Taira 2024; Rolandi *et al*. 2025; Yeh & Taira 2019; Yeh *et al*. 2020). This work not only applies biglobal input–output analysis to flow over periodic hills, but also directly utilises the tensor product (i.e. Kronecker product) to form differentiation matrices on a tensor product grid (Trefethen 2000). This tensor product approach avoids the Fourier transform of the base flow and the penalty force modelling the solid body (Chavarin & Luhar, 2020; Ran *et al*., 2021), and thus, this approach allows a more straightforward manner to formulate and implement the

https://doi.org/10.1017/flo.2026.10055 Published online by Cambridge University Press



(a) Domain for 3D flow over the periodic hill.

(b) The mask function Γ.

Figure 1. *(a) Illustration of periodic hill geometry with L_x, L_y, L_z as the domain size in streamwise, wall-normal and spanwise directions. (b) The value of the mask function Γ with $\Gamma \to 1$ in the solid domain, $\Gamma \to 0$ in the fluid region and a smooth transition through the solid–fluid interface.*

resolvent operator associated with 2-D base flows. We analyse the forcing and response modes of flow over a periodic hill at various spatiotemporal frequencies and Reynolds numbers to understand the effect of external disturbance on the flow response.

The rest of the paper is organised as follows. We set up our problem of flow over a periodic hill and modelling approach using the VPM in § 2. Section 3 then presents DNS to obtain base flows and validate our VPM. In § 4, we discuss the formulation of the biglobal input–output analysis and present results. We conclude this paper and discuss future directions in § 5.

2. Problem set-up and modelling based on volume penalty method

2.1. Flow over periodic hill

We consider incompressible flow over an idealised periodic hill defined in Cartesian coordinates along the streamwise (x), wall-normal (y) and spanwise (z) directions (figure 1*a*). The velocity vector is denoted as $\mathbf{u} = [u, v, w]^{\mathrm{T}}$, where u, v and w are velocity components in streamwise, wall-normal and spanwise directions, respectively. Here, the superscript $^{\mathrm{T}}$ denotes the transpose, and p denotes the pressure. The dynamics of fluid flow is governed by the incompressible Navier–Stokes equations:

$$\frac{\partial \mathbf{u}}{\partial t} + \mathbf{u} \cdot \nabla \mathbf{u} = -\nabla p + \frac{1}{Re}\nabla^2 \mathbf{u} + \mathbf{F} + \mathbf{f}, \qquad \nabla \cdot \mathbf{u} = 0. \tag{2.1}$$

Here, $\mathbf{F}$ is a linear damping penalty term to model the solid domain and $\mathbf{f}$ is the input forcing term that will be used in input–output analysis in § 4, which can represent the free-stream disturbance, experimental uncertainty, background noise and model uncertainty. Here, the length is normalised by the maximal height of the periodic hill H and the velocity is normalised by the bulk velocity U_b^*, which leads to the Reynolds number defined as $Re = U_b^* H/\nu$ with ν as the kinematic viscosity.

We consider a periodic hill geometry with non-dimensional height (Fischer *et al*. 2007) as $y_{\mathrm{hill}}(x) = 3C[1 + \tanh(B(|x - A| - B))]$, where $A = 4.5$, $B = 3.5$ and $C = 1/6$. The hill has a width along the streamwise direction at its base that is two times the maximal height of the hill. We consider a wall-normal domain as $y \in [0, 3]$ and a streamwise domain as $x \in [0, 9]$. We choose such periodic hill geometry and computation domain to be consistent with the problem set-up of the flow over the periodic hill example in Nek5000 software (Fischer *et al*. 2007). This helps us with validating our results against Nek5000, described later in § 3.

2.2. Volume penalty method

Here, we employ an improved VPM (Hester *et al*. 2021) to model the solid domain of a periodic hill. This VPM allows us to employ the same modelling approach for both DNS and input–output analysis (Chavarin & Luhar 2020; Ran *et al*. 2021). The domain Ω is partitioned into Ω_f for the fluid part and

https://doi.org/10.1017/flo.2026.10055 Published online by Cambridge University Press

Ω_s for the solid part of the domain, as shown in figure 1(*b*). The fluid–solid interface is given as $\partial\Omega$, and the VPM aims to impose no-slip and no-penetration boundary conditions at this interface, i.e. $\mathbf{u}|_{\partial\Omega} = \mathbf{0}$.

We employ the penalty forcing term $\mathbf{F}$ in the momentum equation in (2.1) as a linear damping term:

$$\mathbf{F} = -\frac{\Gamma}{\eta}(\mathbf{u} - \mathbf{u}_{\text{solid}}), \tag{2.2}$$

where $\mathbf{u}_{\text{solid}} = \mathbf{0}$ as we consider a stationary periodic hill. In (2.2), Γ is the normalised mask function and η is the non-dimensional damping time scale. The mask function $\Gamma : \Omega \to [0, 1]$ is employed to locate the solid object and the interface in the domain (Hester *et al*. 2021), where $\Gamma = 1$ in the solid domain and $\Gamma = 0$ in the fluid domain with a smooth transition at the solid–fluid interface. Here, we generate the mask function by selecting a normalised mask function $\hat{\Gamma}$, which has to satisfy certain important properties (Hester *et al*. 2021): (i) boundedness: $\hat{\Gamma} : \mathbb{R} \to [0, 1]$; (ii) smoothness: at least C^1 continuous; (iii) limiting behaviour: $\lim_{x\to-\infty} \hat{\Gamma}(x) = 1$ and $\lim_{x\to\infty} \hat{\Gamma}(x) = 0$; (iv) monotonicity: $x_2 > x_1 \Rightarrow \hat{\Gamma}(x_2) < \Gamma(x_1)$; and (v) symmetry: $\hat{\Gamma}(x) + \hat{\Gamma}(-x) = 1$. We choose an error function as the normalised mask function $\hat{\Gamma}_{\text{erf}}$ to satisfy the conditions we listed (Hester *et al*. 2021):

$$\hat{\Gamma}_{\text{erf}}(d_\perp) = \tfrac{1}{2}(1 - \text{erf}(\sqrt{\pi}\, d_\perp)), \tag{2.3}$$

where $\text{erf}(x)$ is the error function $\text{erf}(x) = (2/\sqrt{\pi}) \int_0^x \text{e}^{-t^2}\, \text{d}t$. In (2.3), $d_\perp$ is the signed distance from the boundary of the periodic hill, which is defined as the distance of any point on the grid to the closest point p on the interface $\partial\Omega$. We have $d_\perp > 0$ for the fluid domain, $d_\perp < 0$ for the solid domain and $d_\perp = 0$ at the solid–fluid interface. Then, we can construct our mask function using $\hat{\Gamma}_{\text{erf}}$ as

$$\Gamma(d_\perp) = \hat{\Gamma}_{\text{erf}}\left(\frac{d_\perp}{\delta^*}\right), \tag{2.4}$$

where δ^* is the optimum thickness of the numerical interface.

We discuss how we choose η in (2.2) and δ^* in (2.4) used in the VPM following Hester *et al*. (2021). Here, the non-dimensional damping time scale η is defined as $\eta = \tau U_b^*/H$, where τ is the dimensional damping time scale. We also introduce the non-dimensional damping length scale $\epsilon = \sqrt{\nu\tau}/H$. Here, η measures the ratio of damping and inertial time scales, and ϵ is the ratio of the viscous length and the damping length scale, which are related to each other by $\eta = Re\epsilon^2$. The damping time scale η and length scale ϵ have a strong correlation, and they are equal to each other when $\eta = \epsilon = 1/Re$ (Hester *et al*. 2021). Based on the relation between η and ϵ, either the damping time scale or the length scale dominates the other, leading to various model errors (Hester *et al*. 2021). When $\epsilon > \eta$, the damping is strongest, resulting in second-order convergence, while $\eta > \epsilon$ corresponds to intermediate damping. To reduce free parameters in the VPM, we select the $\eta = \epsilon = 1/Re$ regime where the damping length scale and time scale are equal to each other, which is between the strong damping and the intermediate damping regimes (Hester *et al*. 2021). According to Hester *et al*. (2021), we choose the optimal interface thickness $\delta^* = 3.1134\epsilon$, which leads to $O(\epsilon^2)$ convergence in the strong damping regime as an improvement on previous VPM frameworks (Angot 1999; Carbou and Fabrie 2003). The value of Γ associated with this optimal interface thickness δ^* is shown in figure 1(*b*).

3. Direct numerical simulation to obtain base flow

Here, we implement the VPM described in § 2.2 into the spectral solver Dedalus (Burns *et al*. 2020), and we refer to this implementation as Dedalus-VPM. We then use Dedalus-VPM to obtain the 2-D time-averaged base flow $\mathbf{U} = [U(x, y), V(x, y), 0]^{\text{T}}$ that will be used for the input–output analysis in § 4. We impose periodic boundary conditions in the streamwise direction and impose Dirichlet boundary conditions for the velocity field at the bottom and top of the domain, i.e. $\mathbf{u}(x,\ y = 0,\ t) = \mathbf{u}(x,\ y = L_y,\ t) = \mathbf{0}$. We discretise (2.1) using the Fourier spectral method in the streamwise direction and the Chebyshev spectral method in the wall-normal direction. For simulation results in this section, the input forcing $\mathbf{f}$ in (2.1) is set to zero. As we normalise the velocity scale by the bulk velocity U_b^*, we have

https://doi.org/10.1017/flo.2026.10055 Published online by Cambridge University Press

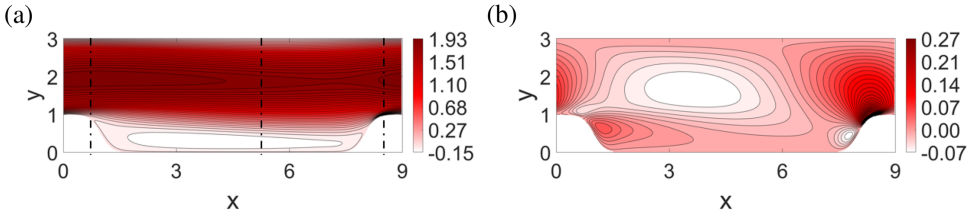


Figure 2. *Steady-state flow (a) $U(x, y)$ and (b) $V(x, y)$ obtained from Dedalus-VPM at $Re = 100$.*

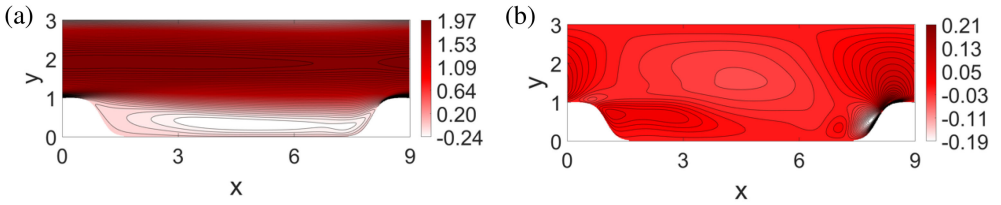


Figure 3. *Time-averaged flow (a) $U(x, y)$ and (b) $V(x, y)$ obtained from Dedalus-VPM at $Re = 190$.*

the non-dimensional bulk velocity as $U_b = 1$. This bulk velocity is imposed by setting the flow rate $Q := \int_{\Omega_f} u(x, y, z, t)\, \mathrm{d}A$ as $Q = U_b|\Omega_f|$ in simulation, where $|\Omega_f|$ denotes the area of the fluid domain. Using bulk velocity as a constraint allows the pressure gradient to vary dynamically while ensuring that the simulation runs at the desired Reynolds number defined by the bulk velocity. The statistically steady state obtained from the DNS is then used to compute the time-averaged base flow $\mathbf{U}$.

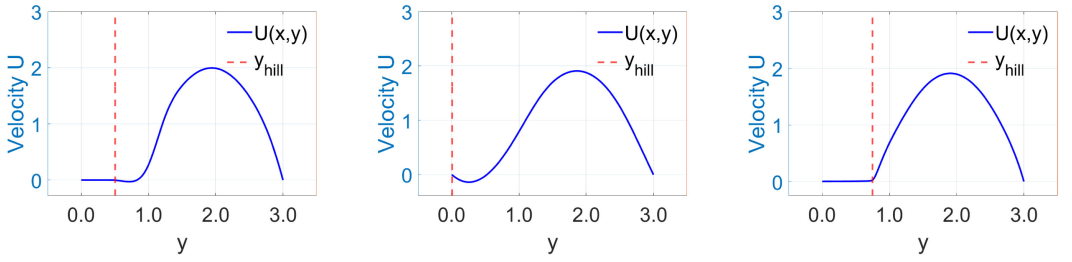
Here, we examine the flow over a periodic hill at $Re = 100$. We use a grid size of $(N_x, N_y) = (352, 512)$ in x and y directions, and the maximum non-dimensional time step is 0.005. At this Reynolds number, the flow remains laminar and will converge to a steady state after the initial transient. Figure 2 shows the steady-state streamwise velocity $U(x, y)$ and wall-normal velocity $V(x, y)$ of flow over a periodic hill using Dedalus-VPM at $Re = 100$. The streamwise velocity in figure 2(a) shows shear-layer formation between low-speed recirculation regions ($y < 0.6$) and the region above the hill ($y > 1$) with a higher velocity. The wall-normal velocity $V(x, y)$ in figure 2(b) shows an upward motion near the hill crest ($x \approx 8$) and a downward motion near $x \approx 4$. We observe a large recirculation bubble downstream of the hill, and the recirculation bubble is stable at this Reynolds number. Flow separation occurs close to the top of the downstream side of the hill ($x \approx 1$), creating recirculation, and the flow gets quicker downstream as it approaches the hill crest at $x = 9$.

Now we look at the unsteady case of $Re = 190$, where the flow is found to be unsteady. According to Breuer *et al*. (2009), flow at $Re = 200$ is unsteady and shows three-dimensional effects after the initial transient of 2-D flow. We select $Re = 190$ to be close to but lower than this $Re = 200$ value to minimise the impact of spanwise motion not included in our 2-D simulations. A grid of $(N_x, N_y) = (384, 576)$ has been chosen for the Dedalus-VPM model. From the time-averaged mean flow profile $U(x, y)$ in figure 3, we still observe the flow separation and reattachment downstream of the hill from the time-averaged velocity, although the recirculation bubble is unsteady.

3.1. Implementation of no-slip boundary conditions

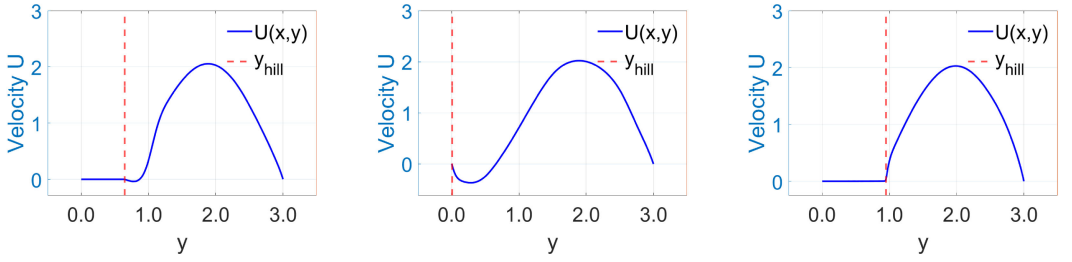
To ensure the fidelity of the fluid–solid interface modelled by the VPM, we examine whether the no-slip boundary condition has been met at the boundary of the periodic hill. Figure 4 shows streamwise velocities at three cross-sections outlined as vertical dashed–dotted lines in figure 2. This also provides insights into the flow separation and recirculation in the valley downstream of the hill. Figure 4 shows that at each cross-section ($x = 0.997$, 5.088 and 8.156), the streamwise velocity $U(x, y) = 0$ at $y_{\mathrm{hill}}(x)$, which indicates that the VPM can effectively implement the no-slip boundary conditions at the boundary of the periodic hill. The velocity $U = 0$ is imposed firmly in the solid region (i.e. the left of the red dashed

https://doi.org/10.1017/flo.2026.10055 Published online by Cambridge University Press



(a) $x = 0.997$ (b) $x = 5.088$ (c) $x = 8.156$

Figure 4. *Steady-state streamwise velocity $U(x, y)$ and $y_{hill}(x)$ at three streamwise locations with $Re = 100$: (a) $x = 0.997$, (b) $x = 5.088$ and (c) $x = 8.156$.*



(a) $x = 0.914$ (b) $x = 4.664$ (c) $x = 8.414$

Figure 5. *Streamwise velocity $U(x, y)$ at $t = 800$ and $y_{hill}(x)$ at three streamwise locations with $Re = 190$: (a) $x = 0.914$, (b) $x = 4.664$ and (c) $x = 8.414$.*

line in figure 4). In figure 4(a), we observe no slip at the hill surface (red dashed line), and streamwise velocity slightly decreases as y increases crossing the recirculation region. At $y > 1$ in the fluid domain, the velocity shows an expected parabolic profile. In figure 4(b) ($x = 5.088$), we see a stronger negative velocity within the recirculation region than in figure 4(a) ($x = 0.997$) due to a strong recirculation observed downstream of the hill. At the third location ($x = 8.156$) shown by figure 4(c), the velocity increases from zero and follows a nearly parabolic profile in the fluid domain. We also look at unsteady flow at $Re = 190$ shown in figure 5, and we are able to establish no slip in this regime as well. The flow profile also shows that the recirculation is stronger downstream at higher Re.

3.2. Validation: Dedalus-VPM versus Nek5000

To validate the VPM against a benchmark numerical framework, we compare the Dedalus-VPM model with the flow over periodic hill results obtained from Nek5000 (Fischer *et al*. 2007). Nek5000 is a spectral element solver with a body-fitting mesh near the boundary of the hill. We choose $Re = 100$ and $Re = 190$ for comparing Dedalus-VPM (Burns *et al*., 2020) and Nek5000 results of flow over the same periodic hill geometry. The mesh size considered for Nek5000 involves 52 elements in x and 24 elements in y, corresponding to a grid size of $(N_x, N_y) = (416, 192)$. The steady-state velocity $U(x, y)$ and $V(x, y)$ at $Re = 100$ and time-averaged velocity at $Re = 190$ obtained from Nek5000 are presented in Appendix A, which shows the same flow features compared with the results obtained by Dedalus-VPM in figures 2 and 3. Moreover, we computed the relative error between these two approaches as $\frac{\sqrt{\overline{(U_{\mathrm{Nek}}-U_{\mathrm{Dedalus}})^2+(V_{\mathrm{Nek}}-V_{\mathrm{Dedalus}})^2}}}{\sqrt{\overline{U_{\mathrm{Nek}}^2+V_{\mathrm{Nek}}^2}}}$. Here, the overline $\overline{(\cdot)}$ means the average over the fluid domain Ω_f, and we interpolate Nek5000 results to the Dedalus grid before computing the relative error. We obtained a relative error computed as 0.09% for the steady-state flow at $Re = 100$ and a relative error of 0.07% for

https://doi.org/10.1017/flo.2026.10055 Published online by Cambridge University Press

the time-averaged flow at $Re = 190$. To further assess the numerical accuracy of the VPM, we conducted a sensitivity analysis at $Re = 100$ by varying the interface parameters ϵ over 20 % to include both $\epsilon < \eta$ and $\epsilon > \eta$ regimes, where the relative error of laminar velocity remains within 0.1 % compared with Nek5000.

4. Input–output analysis of flow over a periodic hill

4.1. Formulation of biglobal input–output analysis

Here, we formulate the biglobal input–output analysis of flow over a periodic hill. We consider a base flow with $\mathbf{U} = [U(x, y), V(x, y), 0]^{\mathrm{T}}$ obtained from the steady-state response or time-averaged mean flow at the statistically steady state obtained from DNS of flow over the periodic hill with the VPM in § 3. We then decompose the velocity into the base flow and the fluctuations around this base flow $\mathbf{u} = \mathbf{U} + \mathbf{u}'$, where $\mathbf{u}' = [u', v', w']^{\mathrm{T}}$. Pressure is also decomposed similarly as $p = P + p'$. After substituting this decomposition in (2.1) and dropping the nonlinear fluctuation–fluctuation interaction terms, we can obtain the linearised equation governing fluctuations as

$$\frac{\partial u'}{\partial t} + U\frac{\partial u'}{\partial x} + V\frac{\partial u'}{\partial y} + u'\frac{\partial U}{\partial x} + v'\frac{\partial U}{\partial y} = -\frac{\partial p'}{\partial x} + \frac{1}{Re}\nabla^2 u' - \frac{\Gamma}{\eta}u' + f_x, \tag{4.1a}$$

$$\frac{\partial v'}{\partial t} + U\frac{\partial v'}{\partial x} + V\frac{\partial v'}{\partial y} + u'\frac{\partial V}{\partial x} + v'\frac{\partial V}{\partial y} = -\frac{\partial p'}{\partial y} + \frac{1}{Re}\nabla^2 v' - \frac{\Gamma}{\eta}v' + f_y, \tag{4.1b}$$

$$\frac{\partial w'}{\partial t} + U\frac{\partial w'}{\partial x} + V\frac{\partial w'}{\partial y} = -\frac{\partial p'}{\partial z} + \frac{1}{Re}\nabla^2 w' - \frac{\Gamma}{\eta}w' + f_z, \tag{4.1c}$$

$$\frac{\partial u'}{\partial x} + \frac{\partial v'}{\partial y} + \frac{\partial w'}{\partial z} = 0. \tag{4.1d}$$

In (4.1*a–c*), f_x, f_y and f_z are each component of the input forcing term $\mathbf{f}$ in (2.1), i.e. $\mathbf{f} = [f_x, f_y, f_z]^{\mathrm{T}}$. The fluctuations satisfy the periodic boundary conditions in the streamwise and spanwise directions, and we also have $\mathbf{u}'(x,\ y = 0, z,\ t) = \mathbf{u}'(x,\ y = L_y, z,\ t) = \mathbf{0}$.

We then perform the normal mode ansatz for fluctuations in the spanwise direction and temporal domain, such that $\phi'(x, y, z, t) = \widehat{\phi}(x, y; k_z, \omega)\exp(\mathrm{i}k_z z + \mathrm{i}\omega t)$ with $\phi = u, v, w, p$. Then, the linearised equation of fluctuations in (4.1) can be formulated as an input–output system:

$$\mathrm{i}\omega\mathbf{E}\Psi = \mathbf{A}\Psi + \mathbf{B}\widehat{\mathbf{f}}, \qquad \widehat{\mathbf{u}} = \mathbf{C}\,\Psi, \tag{4.2}$$

where $\Psi = [\widehat{u}, \widehat{v}, \widehat{w}, \widehat{p}\,]^{\mathrm{T}}$ is the state variable vector and the output vector $\widehat{\mathbf{u}} = [\widehat{u}, \widehat{v}, \widehat{w}]$ is chosen as the Fourier transform of the velocity vector. Here, the $\mathbf{A}$ operator in (4.2) is defined as

$$\mathbf{A} = \begin{bmatrix} A_{11} & -\partial_y U & 0 & -\partial_x \\ -\partial_x V & A_{22} & 0 & -\partial_y \\ 0 & 0 & A_{33} & -\mathrm{i}k_z \\ -\partial_x & -\partial_y & -\mathrm{i}k_z & 0 \end{bmatrix}, \tag{4.3}$$

where

$$A_{11} = -U\partial_x - V\partial_y - \partial_x U + \frac{1}{\mathrm{Re}}\nabla^2 - \frac{\Gamma}{\eta}, \tag{4.4a}$$

$$A_{22} = -U\partial_x - V\partial_y - \partial_y V + \frac{1}{\mathrm{Re}}\nabla^2 - \frac{\Gamma}{\eta}, \tag{4.4b}$$

$$A_{33} = -U\partial_x - V\partial_y + \frac{1}{\mathrm{Re}}\nabla^2 - \frac{\Gamma}{\eta}. \tag{4.4c}$$

https://doi.org/10.1017/flo.2026.10055 Published online by Cambridge University Press

The $\mathbf{B}$, $\mathbf{C}$ and $\mathbf{E}$ operators in (4.2) are defined as

$$\mathbf{B}=\begin{bmatrix} I & 0 & 0 \\ 0 & I & 0 \\ 0 & 0 & I \\ 0 & 0 & 0 \end{bmatrix}, \quad \mathbf{C}=\begin{bmatrix} I & 0 & 0 & 0 \\ 0 & I & 0 & 0 \\ 0 & 0 & I & 0 \end{bmatrix}, \quad \mathbf{E}=\begin{bmatrix} I & 0 & 0 & 0 \\ 0 & I & 0 & 0 \\ 0 & 0 & I & 0 \\ 0 & 0 & 0 & 0 \end{bmatrix}. \tag{4.5}$$

We can then obtain the spatiotemporal frequency response operator $\mathcal{H}$ that maps the input forcing term to the output velocity vector at each spatiotemporal frequency (k_z,ω): $\widehat{\mathbf{u}}(x,y;k_z,\omega)=\mathcal{H}\widehat{\mathbf{f}}(x,y;k_z,\omega)$, where the spatiotemporal frequency response operator $\mathcal{H}$ is given by

$$\mathcal{H}(x,y;k_z,\omega)=\mathbf{C}(\mathrm{i}\omega\mathbf{E}-\mathbf{A})^{-1}\mathbf{B}. \tag{4.6}$$

Here, the spatiotemporal frequency response operator $\mathcal{H}(x,y;k_z,\omega)$ contains differentiation operators in both x and y directions, and $\mathcal{H}(x,y;k_z,\omega)$ also depends on the parameters of spanwise wavenumber k_z and temporal frequency ω. We then perform the singular value decomposition of the spatiotemporal frequency response operator $\mathcal{H}$ to identify the external disturbance (forcing mode) leading to the most amplified flow structures (response mode) and associated energy amplification or energy gain measured by the associated singular value.

4.2. Numerical method

In order to perform singular value decomposition of the spatiotemporal frequency response operator $\mathcal{H}$, we need to conduct numerical discretisation in streamwise x and wall-normal y directions. We employ the Fourier collocation method with N_x grid points in the streamwise direction and employ the Chebyshev collocation method with N_y grid points in the wall-normal direction. As a result, ∂_x will be discretised as a Fourier differentiation matrix $\mathbf{d}_x\in\mathbb{R}^{N_x\times N_x}$ using `fourdif` function and ∂_y will be discretised as a Chebyshev differentiation matrix $\mathbf{d}_y\in\mathbb{R}^{N_y\times N_y}$ using `chebdif` function (Weideman & Reddy 2000). We then directly construct differentiation matrices $\mathbf{D}_x\in\mathbb{R}^{N_xN_y\times N_xN_y}$ and $\mathbf{D}_y\in\mathbb{R}^{N_xN_y\times N_xN_y}$ on the tensor product grid (Julien & Watson 2009; Trefethen 2000):

$$\mathbf{D}_y=\mathbf{I}_x\otimes\mathbf{d}_y, \quad \mathbf{D}_x=\mathbf{d}_x\otimes\mathbf{I}_y, \tag{4.7}$$

where $\mathbf{I}_x\in\mathbb{R}^{N_x\times N_x}$ and $\mathbf{I}_y\in\mathbb{R}^{N_y\times N_y}$ are the identity matrices and $\otimes$ denotes the tensor product, i.e. Kronecker product. We can similarly construct the second-order differentiation matrices by tensor product: $\mathbf{D}_{yy}=\mathbf{I}_x\otimes\mathbf{d}_{yy}$ and $\mathbf{D}_{xx}=\mathbf{d}_{xx}\otimes\mathbf{I}_y$, where $\mathbf{d}_{xx}$ and $\mathbf{d}_{yy}$ are differentiation matrices directly obtained from `fourdif` and `chebdif` (Weideman & Reddy 2000) to numerically approximate second-order differentiations ∂_{xx} and ∂_{yy}. The resulting discretised spatiotemporal response operator $\mathbf{H}$ (i.e. discretisation of $\mathcal{H}$ in (4.6)) will be a matrix with size as $\mathbf{H}\in\mathbb{C}^{3N_xN_y\times 3N_xN_y}$.

Our approach is different from that employed to study flow over riblets (Chavarin & Luhar 2020; Ran *et al*. 2021), as our approach does not need to perform the Fourier transformation of the base flow and the penalty forcing term in the VPM, but directly works on the physical domain (x,y) to incorporate 2-D base flow and geometry into the spatiotemporal frequency response operator. In this approach it is easier to implement the discretised spatiotemporal frequency response operator, and it is also easier to analyse forcing and response modes in the physical domain. Note that the penalty forcing term $\mathbf{F}$ will enforce that both forcing mode $\widehat{\mathbf{f}}$ and response mode $\widehat{\mathbf{u}}$ are close to zero value within the solid domain. We also conducted a sensitivity analysis of selected results and found that the singular values, forcing modes and response modes are robust by varying the interface parameter ϵ within the VPM by 20 %. We then perform singular value decomposition of the discretised spatiotemporal frequency response operator $\mathbf{H}$ over a range of spatiotemporal frequencies and Reynolds numbers. In order to improve the computational efficiency, we utilise the MATLAB command `svds` to compute only the maximum singular value and associated singular vectors to determine the largest amplification and associated forcing and response modes. Here, we use a grid with $(N_x,N_y)=(96,120)$, and thus, explicitly forming the full matrix $\mathbf{H}$ can be memory-intensive.

https://doi.org/10.1017/flo.2026.10055 Published online by Cambridge University Press

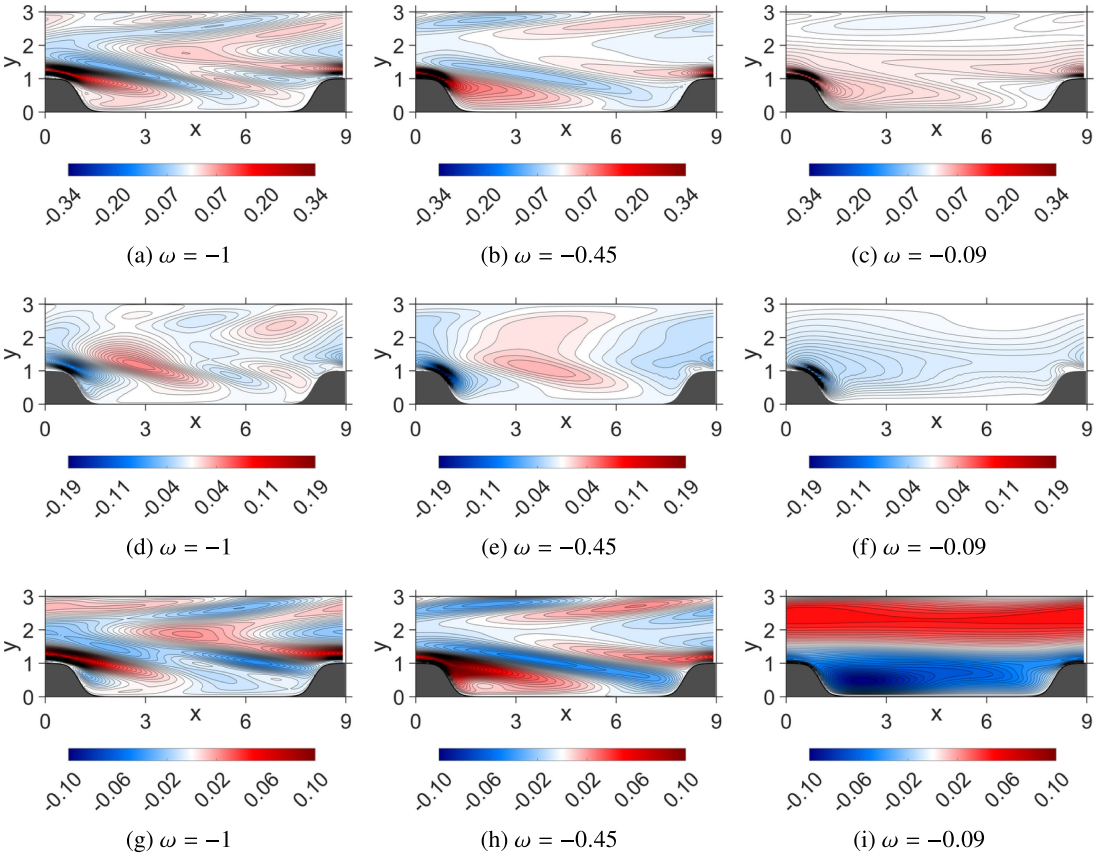


Figure 6. *(a–c) Streamwise forcing modes $\widehat{f_x}(x, y)$. (d–f) Wall-normal forcing modes $\widehat{f_y}(x, y)$. (g–i) Spanwise forcing modes $\widehat{f_z}(x, y)$. All panels are associated with spanwise wavenumber $k_z = 0.55$ and $Re = 100$.*

To reduce the required memory resources, we formulate **A**, **B**, **C**, **E** and **H** matrices using the sparse matrix structures in MATLAB.

4.3. Results of input–output analysis

This subsection shows the results of the input–output analysis. In general, the forcing and response modes are complex, and we only show their real part here because they can be multiplied by an arbitrary complex phase angle $e^{i\theta}$ together and still satisfy the linear input–output mapping. Figure 6(*a–c*) shows streamwise forcing modes $\widehat{f_x}(x, y)$ at spanwise wavenumber $k_z = 0.55$ and three different temporal frequencies $\omega = -1$, -0.45 and -0.09. Here, we observe elongated structures in streamwise forcing mode that tilt in the downstream direction. The strongest streamwise forcing mode, as shown in figure 6, is observed downstream of the hill crest just above the region of recirculation near $x \approx 0.5$ and $y \approx 1$. As the temporal frequency gets closer to zero, we see more organised and larger recirculation zones. For wall-normal forcing modes $\widehat{f_y}(x, y)$ shown in figure 6(*d–f*), the peaks shift to $x \approx 1$ slightly inside the recirculation bubble that forms downstream of the hill, compared with the peak location of streamwise forcing mode shown in figure 6(*a–c*). These observations suggest that imposing streamwise and wall-normal body force near the separation region downstream of the hill crest will be more effective for flow control. Figure 6(*g–i*) then shows the spanwise forcing mode $\widehat{f_z}(x, y)$, where the length scale of the spanwise forcing mode increases as the magnitude of temporal frequency decreases (i.e. $|\omega| \to 0$)

https://doi.org/10.1017/flo.2026.10055 Published online by Cambridge University Press

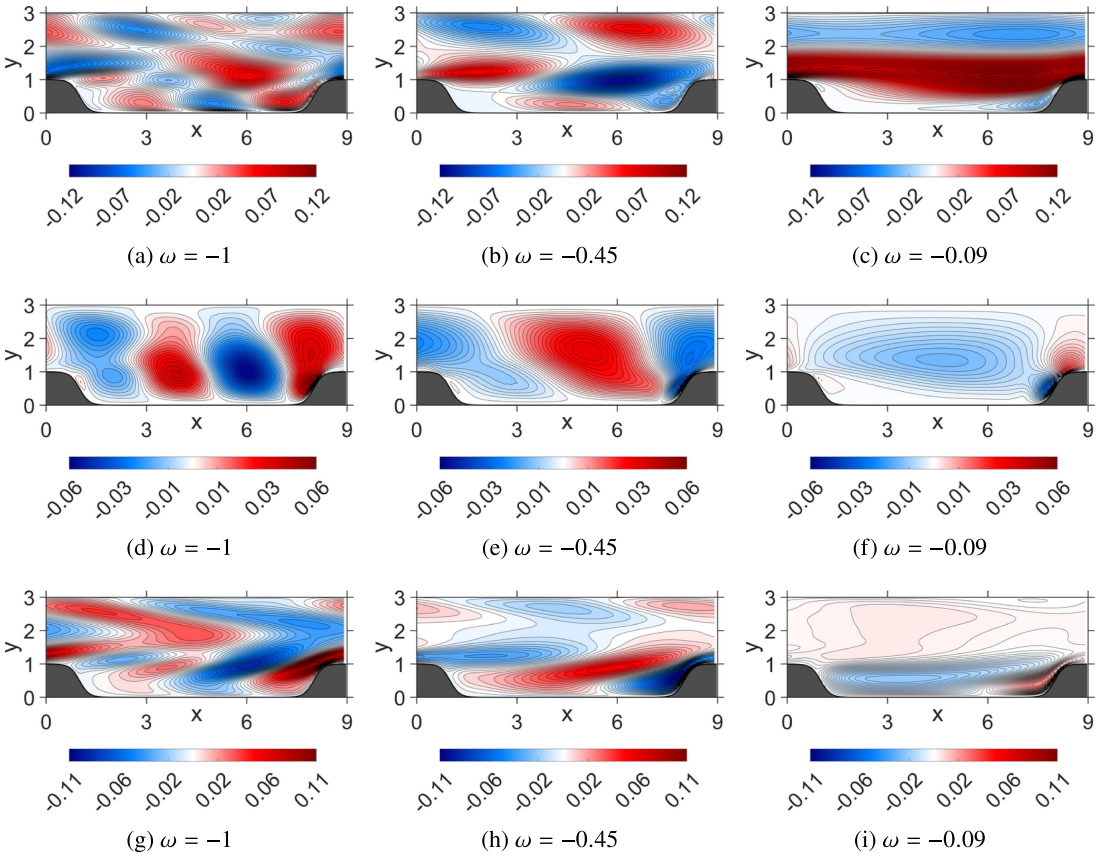


Figure 7. *(a–c) Streamwise response mode $\widehat{u}(x, y)$. (d–f) wall-normal response mode $\widehat{v}(x, y)$. (g–i) Spanwise response mode $\widehat{w}(x, y)$. All panels are associated with $k_z = 0.55$ and $Re = 100$.*

with peak location shifting inside the recirculation region (see figure 6*i*). Comparing the magnitude of forcing modes in three components in figure 6, we found that the streamwise forcing mode is larger than both the wall-normal and spanwise forcing modes, suggesting that perturbing the flow through streamwise body force is more effective for manipulating separated flow over a periodic hill. This is different from the canonical wall-bounded shear flows without flow separation, where cross-stream (wall-normal and spanwise) forcing modes are more effective for amplifying flow responses (Hwang & Cossu 2010; Jovanović & Bamieh 2005) due to the lift-up mechanism (Brandt 2014).

Figure 7 then shows the response modes when the flow is forced by the forcing mode in figure 6. Here, we show how response modes $\widehat{u}(x, y)$, $\widehat{v}(x, y)$ and $\widehat{w}(x, y)$ change over temporal frequency at selected spanwise wavenumber $k_z = 0.55$. From figure 7(*a–c*), we can observe that the streamwise response mode $\widehat{u}(x, y)$ becomes larger in length scale in the streamwise direction as ω goes from -1 to 0. Moreover, the peak of streamwise response modes appears at the middle of the computational domain ($x \approx 6$, $y \approx 1$) at $\omega = -0.45$ (figure 7*b*), while the peak shifts towards the downstream direction near $x = 6$ at $\omega = -0.09$ (figure 7*c*). As the magnitude of frequency approaches zero, the flow becomes less oscillatory in space and resembles the mean flow shown in figure 2. Furthermore, we look at the wall-normal velocity response mode $\widehat{v}(x, y)$ in figure 7(*d–f*). At higher magnitudes of frequency, the wall-normal response mode $\widehat{v}(x, y)$ shows alternating bands (figure 7*d*) resembling separated shear layers (Rolandi *et al*. 2025) observed in the response mode of flow over an aerofoil at high disturbance frequencies. Such alternating feature of wall-normal response mode is also similar to what was observed in the spatial input–output analysis of turbulent boundary layer with a plasma actuator (Liu *et al*. 2022) and resolvent analysis of wind turbine wakes (Li & Yang 2024). As $|\omega|$ decreases, we can see the length scale of the recirculation

https://doi.org/10.1017/flo.2026.10055 Published online by Cambridge University Press

bubble increases as shown in figure 7(*d–f*). Furthermore, figure 7(*g–i*) shows the spanwise response mode $\widehat{w}(x, y)$ whose magnitude also decays as ω is approaching zero. Moreover, the peaks of the wall-normal and spanwise response modes also appear near the reattachment region upstream of the hill crest at $x \approx 8$ as shown in figure 7.

For all of the forcing mode and response mode results in figures 6 and 7, flow structures display a small length scale at high frequency magnitude $|\omega|$, while flow structures show a larger length scale as $\omega \to 0$. This behaviour is similar to the observations obtained from biglobal resolvent analysis of separated flow around an aerofoil (Rolandi *et al*. 2025), where response mode shifts from shear-layer-dominant structures (smaller length scale) at higher frequencies to wake-dominant structures (larger length scale) at lower frequencies. Moreover, the trend that the length scale of flow response will increase as the disturbance frequency decreases is also similar to spatial input–output analysis results of an actuated turbulent boundary layer (Liu *et al*. 2022), resolvent analysis of wind turbine wakes (Li and Yang 2024) and resolvent analysis of cavity flows (Islam & Sun 2024; Liu & Gaitonde 2021; Sun *et al*. 2020). At a temporal frequency close to zero ($\omega \to 0$), the forcing and response modes span the entire streamwise domain (see figures 6*c*, *f*, *i* and 7*c*, *f*, *i*). This is a unique feature due to the streamwise periodicity of flow over a periodic hill, while other separated flows without streamwise periodicity mostly show forcing and response modes concentrated near the separation region (Islam & Sun 2024; Li & Yang 2024; Liu & Gaitonde 2021; Rolandi *et al*. 2024; Sun *et al*. 2020). This observation of forcing and response modes at $\omega \to 0$ for flow over a periodic hill can be used to inform passive flow control or active flow control with steady actuation (Frank-Shapir and Gluzman 2025).

The observed peak values of streamwise forcing modes $\widehat{f_x}$ near the separation region downstream of the hill crest (figure 6) have similarities to the streamwise forcing modes observed in laminar cavity flow (Sun *et al*. 2020). The forcing modes of cavity flow are observed to be concentrated near the leading edge of the cavity, while response modes are observed to peak at downstream regions close to the trailing edge of the cavity (Islam & Sun 2024; Liu & Gaitonde 2021; Sun *et al*. 2020). For flow over a periodic hill, the response modes concentrate near the reattachment region just upstream of the hill crest around $x \approx 8$ (figure 7). Hence, the disturbances created by the forcing downstream of the hill crest have the most amplified response concentrated near the reattachment region. The streamwise periodicity of flow over a periodic hill also allows the coupling between forcing and response modes: disturbances originating from the shear layer shed at the crest of the first hill excite energetic flow responses upstream of the second hill, which in turn trigger energy growth further downstream, leading to disturbances located upstream of the subsequent hill. Such forcing–response interactions reinforce the energy amplification across successive hill-to-hill intervals and potentially lead to the amplified flow structures spanning the entire streamwise domain observed at $\omega \to 0$.

We have analysed the forcing and response modes over different ω with a fixed spanwise wavenumber $k_z = 0.55$. Now, we analyse the impact of changing spanwise wavenumbers. We show streamwise and wall-normal forcing and response modes at $\omega = 1$ with increasing k_z in figures 8 and 9. Here, streamwise forcing mode $\widehat{u}(x, y)$ at lower k_z shows finger-like tilted structures (figure 8*a*), while the streamwise length scale of forcing mode increases as the spanwise wavenumber k_z increases, as shown in figure 8(*c*). We then analyse wall-normal forcing mode with increasing k_z as shown in figure 8(*d–f*). Here, we find that the wall-normal forcing mode is concentrated near the separation region immediately downstream of the hill (near $x \approx 0.5$). At larger k_z (figure 8*f*), the forcing mode becomes of nearly the same magnitude near the hill ($x \approx 0.5$) or in the middle of the domain ($x \approx 4.5$). We then examine the influence of spanwise wavenumber k_z on the response mode shown in figure 9. The streamwise response mode $\widehat{u}(x, y)$ shows small, highly oscillatory behaviour in the spatial domain for small k_z (figures 9*a* and 9*b*), while the streamwise response mode becomes larger and less oscillatory in the streamwise direction at large k_z (figure 9*c*). A similar trend as k_z increases is also observed in wall-normal response mode, as shown in figures 9(*d–f*).

We then examine the influence of changing spanwise wavenumber k_z with temporal frequencies for $\omega = 0.45$ and $\omega = -0.09$. Figures 10 and 11 show that the streamwise and wall-normal response modes increase in length scale, and become smooth as ω gets closer to 0, compared with spatially oscillatory

https://doi.org/10.1017/flo.2026.10055 Published online by Cambridge University Press

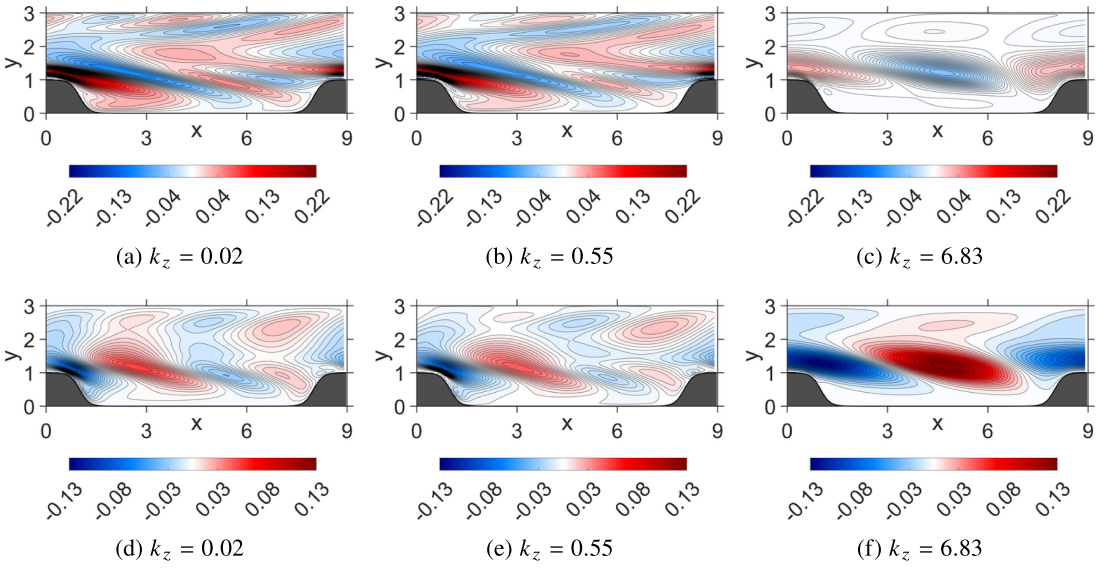


Figure 8. *(a–c) Comparison of streamwise forcing modes $\widehat{f_x}(x, y)$ and (d–f) comparison of wall-normal forcing modes $\widehat{f_y}(x, y)$ over different spanwise wavenumbers. All panels are associated with $Re = 100$ and $\omega = 1$.*

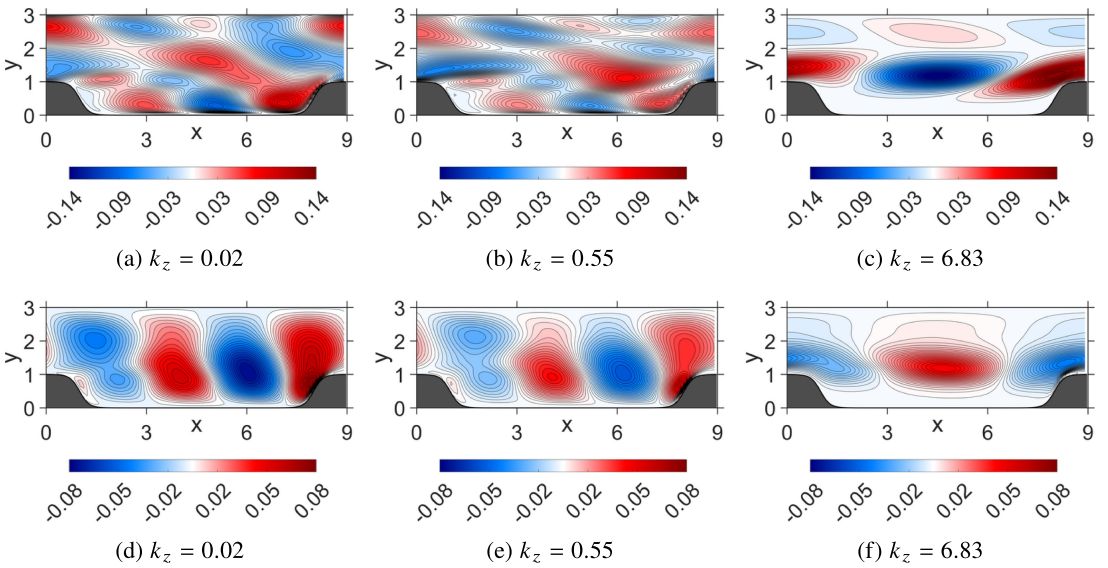
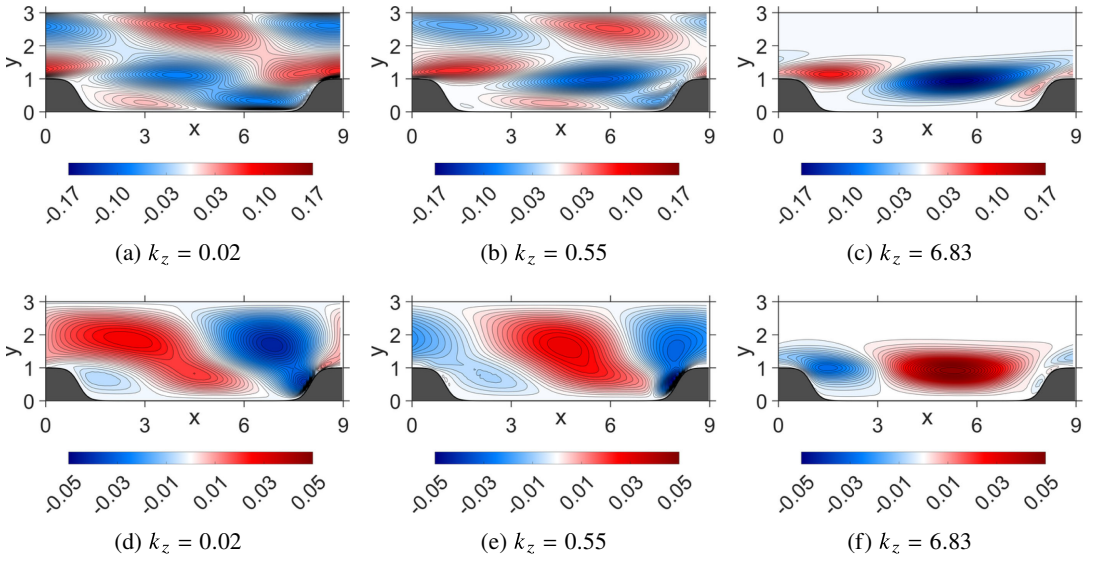


Figure 9. *(a–c) Comparison of streamwise response modes $\widehat{u}(x, y)$ and (d–f) comparison of wall-normal response modes $\widehat{v}(x, y)$ over different spanwise wavenumbers. All panels are associated with $Re = 100$ and $\omega = 1$.*

response modes at $\omega = 1$ (figure 9). At $\omega = 0.45$, the shape of the flow structures is generally preserved over different k_z, except at very high spanwise wavenumbers (figures 10*c* and 10*f*). Hence, at moderate temporal frequencies, the flow is transitioning from being shear-dominant to recirculation-dominant. The response modes at low frequency and low spanwise wavenumbers (figures 11*a* and 11*d*) are similar to the mean flow. Moreover, the variation in spanwise wavenumber does not significantly affect the length scale of the flow structures at $\omega = -0.09$. This implies that low-frequency disturbances with a

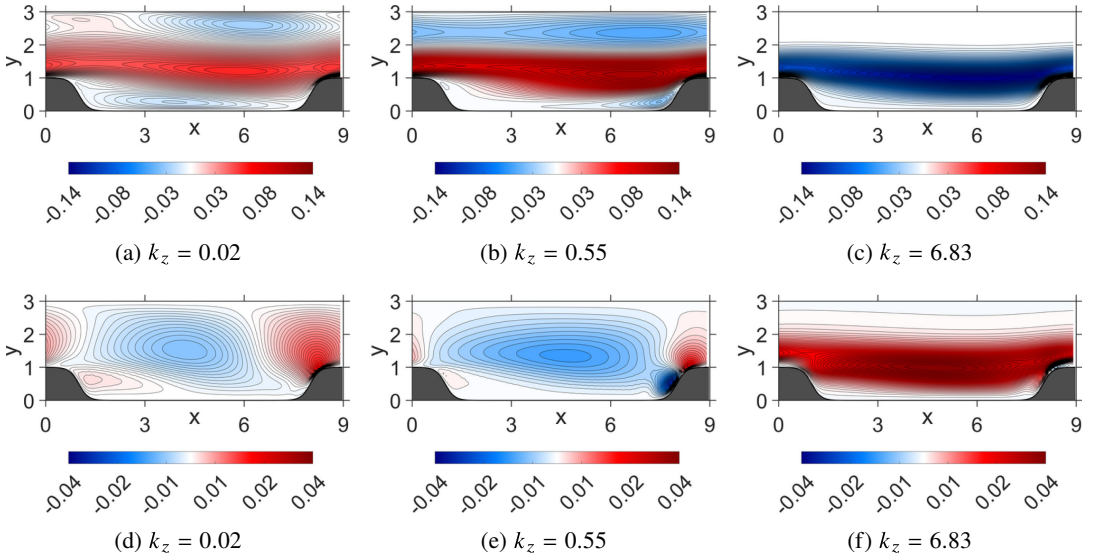
https://doi.org/10.1017/flo.2026.10055 Published online by Cambridge University Press



(a) $k_z = 0.02$ (b) $k_z = 0.55$ (c) $k_z = 6.83$

(d) $k_z = 0.02$ (e) $k_z = 0.55$ (f) $k_z = 6.83$

Figure 10. *(a–c) Comparison of streamwise response modes $\widehat{u}(x, y)$ and (d–f) comparison of wall-normal response modes $\widehat{v}(x, y)$ over different spanwise wavenumbers. All panels are associated with $Re = 100$ and $\omega = 0.45$.*



(a) $k_z = 0.02$ (b) $k_z = 0.55$ (c) $k_z = 6.83$

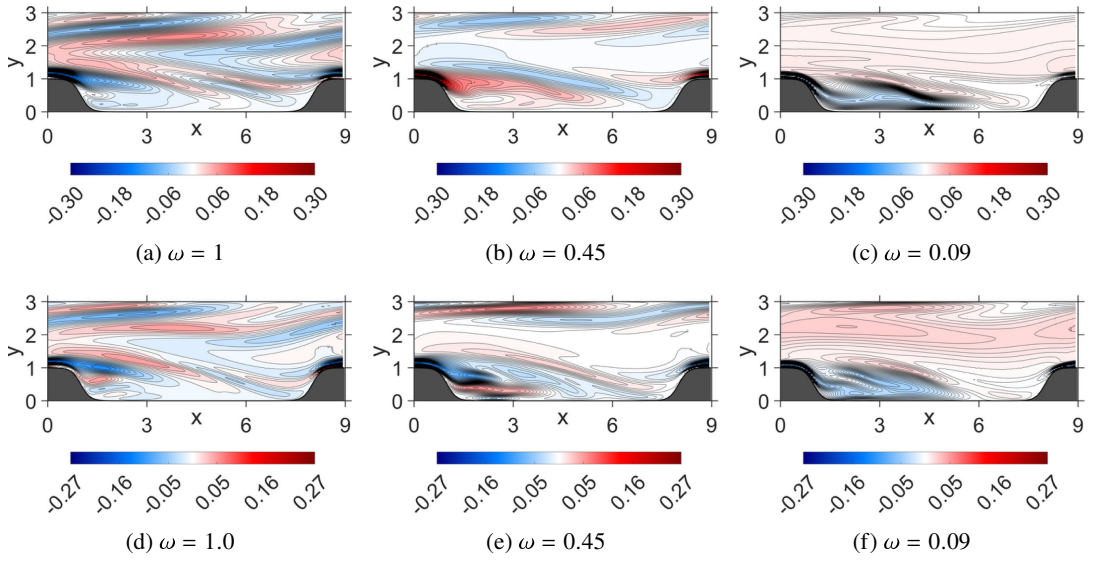
(d) $k_z = 0.02$ (e) $k_z = 0.55$ (f) $k_z = 6.83$

Figure 11. *(a–c) Comparison of streamwise response modes $\widehat{u}(x, y)$ and (d–f) comparison of wall-normal response modes $\widehat{v}(x, y)$ over different spanwise wavenumbers. All panels are associated with $Re = 100$ and $\omega = -0.09$.*

wide range of spanwise wavenumbers are likely to induce large-scale response modes spanning the entire streamwise and wall-normal directions. As k_z increases, the wall-normal response mode is varied, and shows overall shape similar to that of the streamwise response mode at $k_z = 6.83$ and $\omega = -0.09$ (see figures 11*c* and 11*f*).

After analysing forcing and response modes in the laminar regime at $Re = 100$, we conduct input–output analysis of the flow over a periodic hill at $Re = 190$ and $Re = 300$ over a range of temporal frequencies (ω) with spanwise wavenumber $k_z = 0.55$ (figures 12 and 13). The Dedalus-VPM

https://doi.org/10.1017/flo.2026.10055 Published online by Cambridge University Press



(a) $\omega = 1$ (b) $\omega = 0.45$ (c) $\omega = 0.09$

(d) $\omega = 1.0$ (e) $\omega = 0.45$ (f) $\omega = 0.09$

Figure 12. *Comparison of streamwise forcing modes* $\widehat{f_x}(x, y)$ *at* $Re = 190$ *and* $Re = 300$ *over a range of reducing temporal frequencies* $\omega = 1$*, 0.45, and 0.09. (a–c) Streamwise forcing modes* $\widehat{f_x}(x, y)$ *at* $Re = 190$ *and (d–f) streamwise forcing modes* $\widehat{f_x}(x, y)$ *at* $Re = 300$*. All panels are associated with* $k_z = 0.55$*.*

simulations show that the flow over a periodic hill is unsteady at $Re = 190$ and displays chaotic behaviour at $Re = 300$. This comparative analysis over various Reynolds numbers allows us to connect input–output analysis results at low Reynolds numbers with those at higher Reynolds numbers. The input–output analysis has been conducted at grid numbers of $N_x \times N_y = 108 \times 132$ at $Re = 190$, and $N_x \times N_y = 120 \times 168$ at $Re = 300$. Figure 12 compares the shape of the streamwise forcing mode with decreasing ω at $Re = 190$ and $Re = 300$. At $Re = 300$, the peak of forcing modes associated with $\omega = 1$ and $\omega = 0.45$ is strongly confined to the separation region downstream of the hill crest (figure 12*d*, *e*), while the forcing mode extends further downstream at $Re = 190$ (figure 12*a*, *b*), reaching the hill crest at $x = 9$.

Figure 13 presents the streamwise response modes at $Re = 190$ and $Re = 300$. At higher frequencies, response modes are oscillatory in space, shear-dominant and localised as observed in figure 13(*a*, *d*). As ω reduces, flow becomes more recirculation-dominant, spanning the entire spatial domain, a trend similar to observations at $Re = 100$. The similarity of the spatial structures of response modes at low and high Reynolds numbers was also observed in cavity flows (Sun *et al*. 2020). Comparing the streamwise response mode at $Re = 190$ and $Re = 300$, we found that the response mode at $Re = 190$ is attached closely to the hill crest at $x = 9$ (figure 13*b*, *c*), while the response mode at $Re = 300$ is more closely confined to the basin ($x \in [2, 7]$, $y = 0$) between periodic hills (figure 13*e*, *f*), similar to observations in the forcing mode (figure 12).

In figures 14 and 15, we analyse forcing and response modes at $\omega = 1$ over a range of spanwise wavenumbers $k_z = 0$, 1.026 and 2.94 at Reynolds numbers $Re = 190$ and 300. Here, $k_z = 0$ corresponds to spanwise invariant forcing and response. At low k_z, the forcing and response modes penetrate into the basin between periodic hills ($y \leq 1$), while at high k_z, forcing and response modes mostly show non-zero values above the hill peak ($y \geq 1$); see figures 14(*c*) and 15(*c*). A similar dependence on spanwise wavenumber was also shown in resolvent analysis of compressible cavity flows (Sun *et al*. 2020), where response modes at lower spanwise wavenumbers penetrate deeper into the cavity. Comparing results at Reynolds numbers $Re = 190$ and $Re = 300$ in figures 14 and 15, both forcing modes and response modes at $Re = 300$ show meandering behaviour and generation of small secondary recirculations near the separation region ($x \in [1, 3]$ and $y \in [0, 1]$). In cavity flows, small and sizable recirculations in addition to primary recirculation were observed in laminar and turbulent flow regimes (Sun *et al*. 2020), and our

https://doi.org/10.1017/flo.2026.10055 Published online by Cambridge University Press

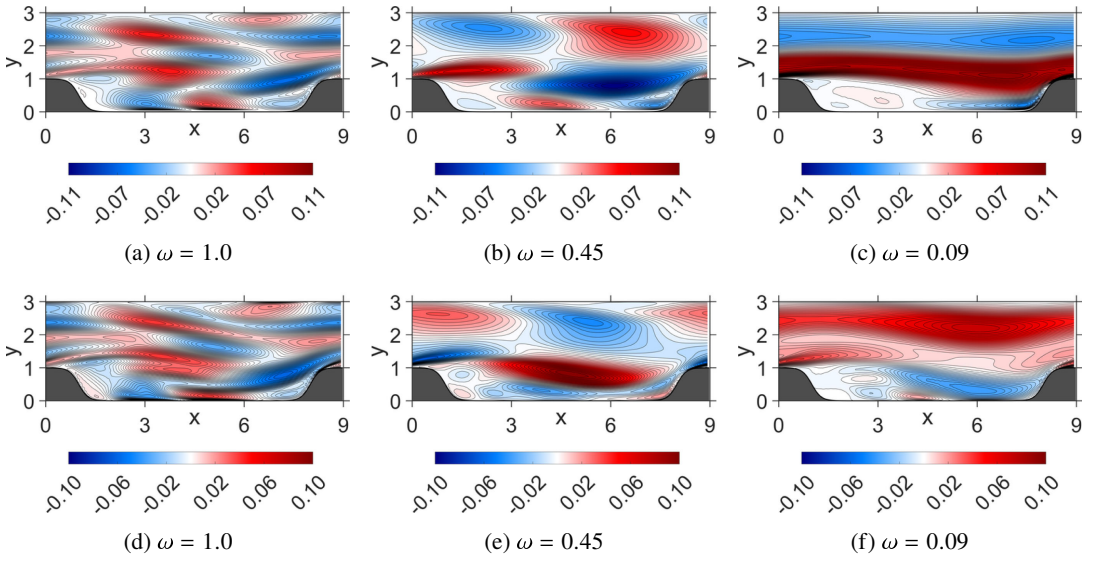


Figure 13. *Comparison of streamwise response modes $\widehat{u}(x, y)$ at $Re = 190$ and $Re = 300$ over temporal frequencies $\omega = 1,\ 0.45$ and 0.09. (a–c) Streamwise response modes $\widehat{u}(x, y)$ at $Re = 190$ and (d–f) streamwise response modes $\widehat{u}(x, y)$ at $Re = 300$. All panels are associated with $k_z = 0.55$.*

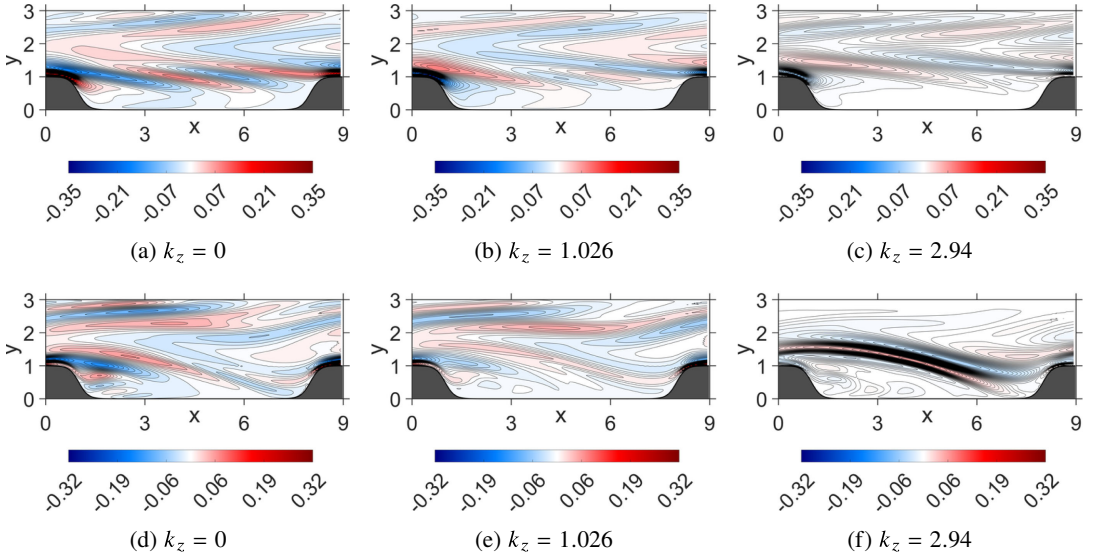
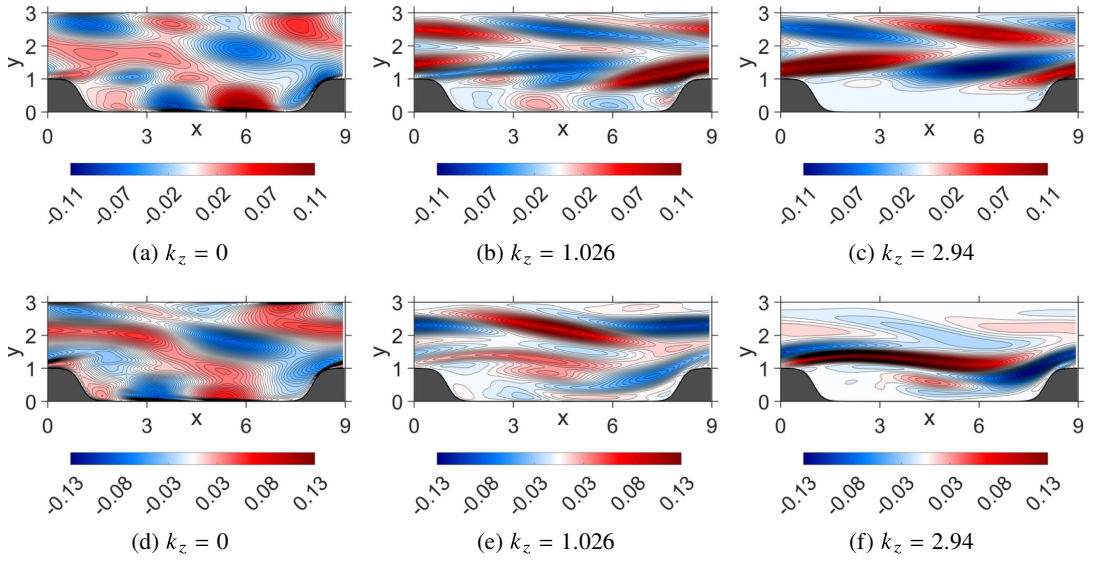


Figure 14. *Comparison of streamwise forcing modes $\widehat{f_x}(x, y)$ at $Re = 190$ and $Re = 300$ over a range of increasing wavenumbers $k_z = 0$, 1.026 and 2.94. (a–c) Streamwise forcing modes $\widehat{f_x}(x, y)$ at $Re = 190$ and (d–f) streamwise forcing modes $\widehat{f_x}(x, y)$ at $Re = 300$. All panels are associated with $\omega = 1$.*

results show that secondary recirculations also appear in forcing and response modes as the Reynolds number increases.

From the above analysis, we can infer that at higher frequencies (or shorter time scales) and moderate spanwise wavenumbers $k_z \in [0.55, 2.94]$, the flow structures are oscillatory in the spatial domain, which is robust for Reynolds numbers $Re = 100$, 190 and 300. In this regime, our response mode of flow over a periodic hill is similar to the shear-dominant structures observed in flow over an aerofoil with high-frequency disturbance (Rolandi *et al*. 2025). As the spanwise wavenumber k_z of disturbance

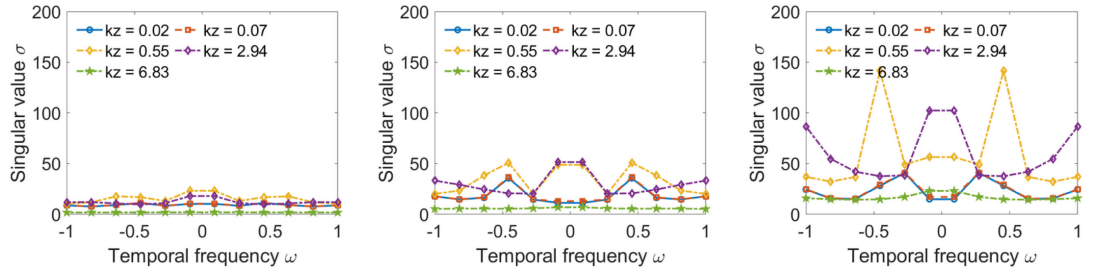
https://doi.org/10.1017/flo.2026.10055 Published online by Cambridge University Press



(a) $k_z = 0$ (b) $k_z = 1.026$ (c) $k_z = 2.94$

(d) $k_z = 0$ (e) $k_z = 1.026$ (f) $k_z = 2.94$

Figure 15. *Comparison of streamwise response modes $\widehat{u}(x, y)$ at $Re = 190$ and $Re = 300$ over a range of increasing wavenumbers $k_z = 0$, 1.026 and 2.94. (a–c) Streamwise response modes $\widehat{u}(x, y)$ at $Re = 190$ and (d–f) streamwise response modes $\widehat{u}(x, y)$ at $Re = 300$. All panels are associated with $\omega = 1$.*



(a) $Re = 50$ (b) $Re = 100$ (c) $Re = 190$

Figure 16. *The largest singular value σ of spatiotemporal frequency response operator $\mathcal{H}$ over temporal frequency for (a) $Re = 50$, (b) $Re = 100$ and (c) $Re = 190$ over spanwise wavenumbers $k_z = [0.02, 0.07, 0.55, 2.94, 6.83]$.*

increases, flow structures become larger and more coherent in streamwise and wall-normal directions, displaying both shear-dominant dynamics and recirculation bubbles. For disturbances with longer time scales or smaller frequencies, we also find that response modes are less oscillatory and more coherent in the spatial domain, displaying large recirculation regions. In general, the forcing mode shows the peak near the separation region downstream of the hill crest, while the response mode shows the peak near the reattachment region upstream of the hill crest.

Figure 16 then shows the largest singular values (σ) representing input–output amplification for various spanwise wavenumber k_z and temporal frequencies ω of disturbance. For temporal frequency ω close to zero, the largest energy amplification is associated with a moderate spanwise wavenumber between $k_z = 0.55$ and $k_z = 2.94$, while at temporal frequency near $\omega = \pm 0.5$, we have the maximal gain obtained at $k_z = 0.55$ for all three Reynolds numbers $Re \in [50, 190]$. At high spanwise wavenumber $k_z = 6.83$, the singular value is close to 0. The peak amplification near $k_z = 0.55$ can be connected to the streamwise length of the recirculation bubble by comparing figure 11(*d–f*). At $k_z = 0.55$ for

https://doi.org/10.1017/flo.2026.10055 Published online by Cambridge University Press

which the amplification is maximum, the wall-normal response mode spans nearly the streamwise distance between periodic hills (figure 11*e*), and spanwise wavelength $\lambda_z = 2\pi/k_z = 11.42$ is close to the distance between periodic hills. At low $k_z = 0.02$, the wall-normal response mode is shorter in the streamwise direction without reaching the downstream hill (figure 11*d*), while at high $k_z = 6.83$, the wall-normal response mode spans the entire domain without the feature of a recirculation bubble (figure 11*f*). Therefore, the observed peak in amplification at moderate k_z may be because large energy amplification can be generated by disturbances associated with streamwise and spanwise length scales close to the distance between periodic hills.

Moreover, we also observe larger amplification as the Reynolds number increases, which is similar to the observations in wall-bounded shear flows that become more sensitive to external disturbance as the Reynolds number increases (Farrell & Ioannou 1993; Jovanović & Bamieh 2005; Jovanović 2021; Liu & Gayme 2021; Trefethen *et al*. 1993).

5. Conclusion

This work conducted a biglobal input–output analysis of separated flow over a periodic hill. The hill is homogeneous in the spanwise direction, and we focus on the laminar and transitional flow regimes at $Re = 100$, $Re = 190$ and $Re = 300$. We use an improved VPM (Hester *et al*. 2021) to model the solid domain in both spectral method solver Dedalus (Burns *et al*. 2020) and input–output analysis. We validate that the steady and time-averaged laminar separated flow obtained from Dedalus-VPM agrees well with results from the spectral element solver Nek5000 (Fischer *et al*. 2007) with a body-fitting grid. The time-averaged velocity obtained from Dedalus-VPM is then used as the base flow within the biglobal input–output analysis. We use the tensor product to obtain differentiation matrices on a tensor product grid, which are then used to formulate our biglobal spatiotemporal frequency response operator. This approach avoids the Fourier transform of the base flow and the penalty forcing in the VPM (Chavarin & Luhar 2020; Ran *et al*. 2021), which allows us to directly analyse forcing and response modes in the physical domain. Singular value decomposition of the spatiotemporal frequency response operator is then conducted to obtain the response mode and forcing mode over a wide range of spanwise wavenumbers and temporal frequencies.

We find that as the magnitude of temporal frequency increases, the flow structures are oscillatory in the spatial domain and have smaller length scales, which resemble shear-dominant structures observed in separated flow over an aerofoil with high-frequency disturbance (Rolandi *et al*. 2025). As the temporal frequency approaches zero ($\omega \to 0$), the response modes are less oscillatory and more coherent in the spatial domain, displaying global recirculation-dominated flow structures. This trend of response mode as increasing temporal frequency is similar to the observations based on resolvent analysis of separated flow over an aerofoil (Rolandi *et al*. 2025), separated flow over a cavity (Islam & Sun 2024; Liu & Gaitonde 2021; Sun *et al*. 2020), actuated turbulent boundary layers (Liu *et al*. 2022) and wind turbine wake (Li & Yang 2024). As the spanwise wavenumber k_z of disturbance increases, flow structures become larger and more coherent in streamwise and wall-normal directions, displaying both shear-dominant dynamics and recirculation bubbles. At both small temporal frequency and small spanwise wavenumber ($\omega \to 0$ and $k_z \to 0$), the response mode is similar to the laminar base flow with domain-filling flow structures. Moreover, the peak locations of the forcing modes appear near the separation region downstream of the hill crest, while the peak locations of the response modes appear near the reattachment region upstream of the hill crest, which is also similar to resolvent analysis of flow over a cavity (Islam & Sun 2024; Liu & Gaitonde 2021; Sun *et al*. 2020). The streamwise periodicity allows coupling between forcing and response modes, which potentially leads to the forcing and response modes spanning the entire streamwise domain at $\omega \to 0$. For input–output amplification measured by the largest singular value, we find that the amplification increases as the spanwise wavenumber increases and reaches peak amplification around $k_z = 0.55$ for $\omega \approx 0.5$. However, a high spanwise wavenumber ($k_z = 6.83$) will lead to a small input–output gain close to zero.

At Reynolds numbers $Re = 190$ and $Re = 300$, the forcing and response modes are influenced by temporal frequency similar to the trend observed at $Re = 100$. At $Re = 190$, the flow is more constrained

https://doi.org/10.1017/flo.2026.10055 Published online by Cambridge University Press

by the geometry of the hill, where the forcing mode at high frequency extends downstream, reaching the periodic hill at $x = 9$ (figure 12). However, at $Re = 300$, the forcing mode is more confined within the separation region downstream of the hill crest, and the response mode is constrained within the basin of periodic hills. Both forcing and response modes show meandering behaviour associated with the generation of small secondary recirculations at $Re = 300$.

In the future, this work can be further extended to triglobal input–output analysis with base flows that depend on three spatial dimensions. Moreover, this biglobal input–output analysis can also be applied to flow over other complex geometries, such as wavy walls, aerofoils and riblets. We also aim to further improve the computational efficiency of our biglobal input–output analysis in the future.

Acknowledgements. The computational work for this project was conducted using resources provided by the Storrs High-Performance Computing (HPC) cluster. We extend our gratitude to the UConn Storrs HPC and its team for their resources and support, which aided in achieving these results. The computational resources for this project were also provided by the NSF ACCESS programme (project number: PHY240243), allowing us to use the Bridges-2 cluster in the Pittsburgh Supercomputing Center.

Data availability statement. Data and code of this paper are publicly available at https://doi.org/10.5281/zenodo.18343671.

Funding statement. This work was supported by the University of Connecticut (UConn) Research Excellence Program (REP). C.L. gratefully acknowledges support from the US National Science Foundation (NSF) through grant number CBET 2542711 during the completion of this work.

Competing interests. The authors declare no conflict of interest.

Ethical standards. The research meets all ethical guidelines, including adherence to the legal requirements of the study country.

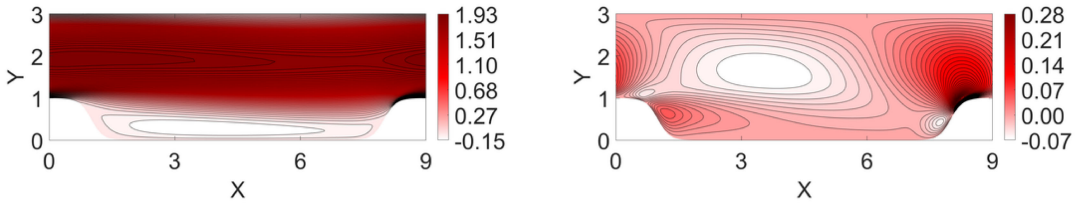
Appendix A. Validation of Dedalus-VPM and grid convergence of input–output analysis

Nek5000 is an open-source computational fluid dynamics solver that solves incompressible Navier–Stokes equations for flow over complex geometries using the spectral element method (Deville *et al*. 2002; Fischer *et al*. 2007). The spectral element method combines the properties of finite element methods with the high-order accuracy of spectral methods (Patera 1984), which is good for achieving very low numerical dissipation and dispersion. Nek5000 uses curvilinear body-fitting high-order polynomial grids near the surface of the geometry over which flow is to be modelled. This makes it a very good tool for performing DNS and large-eddy simulation for laminar, transitional and turbulent flows (Deville *et al*. 2002; Fischer *et al*. 2007). Nek5000 can also solve compressible Navier–Stokes equations and magnetohydrodynamic equations. We have utilised Nek5000 in this paper to provide validation for our Dedalus-VPM model of flow over a periodic hill. Our Nek5000 domain and parameters are the same as the periodic hill domain using Dedalus-VPM in § 3. The results of the steady-state or time-averaged velocity fields from Nek5000 are shown in figures A1 and A2 at, respectively, $Re = 100$ and $Re = 190$, which show the same flow features and velocity magnitude as our Dedalus-VPM model shown in figures 2 and 3.

For validating the grid convergence of the input–output analysis, we have performed a grid convergence study for the same periodic hill domain with VPM as shown in figure 1 at $Re = 100$. We compute the relative error of the streamwise response mode by

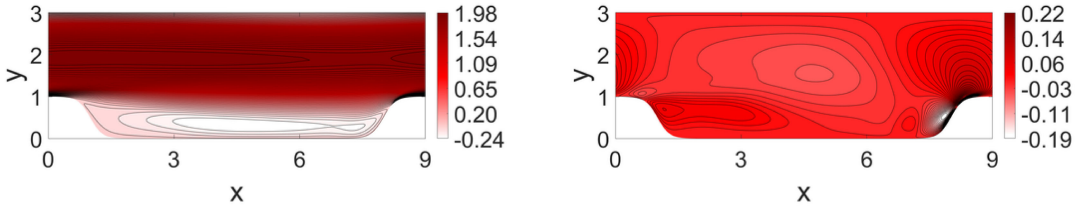
$$\text{Relative error} = \frac{\sqrt{\overline{(\widehat{u}_{\text{coarse}} - \widehat{u}_{\text{fine}})^2 + (\widehat{v}_{\text{coarse}} - \widehat{v}_{\text{fine}})^2}}}{\sqrt{\overline{\widehat{u}^2_{\text{fine}} + \widehat{v}^2_{\text{fine}}}}}. \tag{A1}$$

The relative errors for wall-normal response mode $\widehat{v}$ and spanwise response mode $\widehat{w}$ are computed similarly. We interpolate the results of the most refined grid (Grid 5) with $(N_x \times N_y) = (108 \times 132)$ to each of the coarse grids (Grid 1–Grid 4) to compute such relative error in (A1). Figure A3 shows a



(a) Streamwise velocity $U(x, y)$ (b) Wall-normal velocity $V(x, y)$

Figure A1. *Steady-state velocity fields for flow over a periodic hill computed using Nek5000 at* $Re = 100$.



(a) Streamwise velocity $U(x, y)$ (b) Wall-normal velocity $V(x, y)$

Figure A2. *Time-averaged velocity fields for flow over a periodic hill computed using Nek5000 at* $Re = 190$.

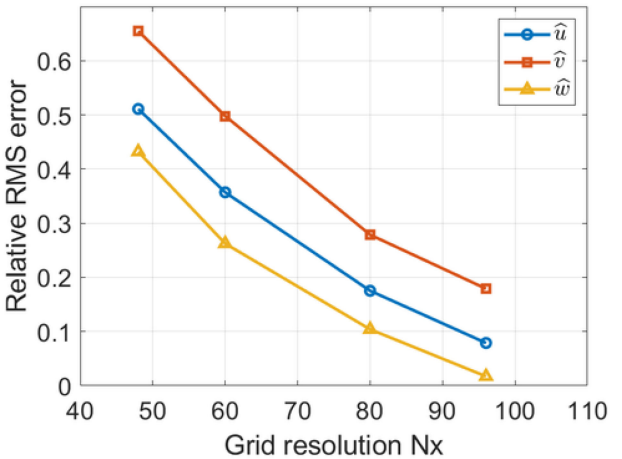


Figure A3. *Relative error of the streamwise response mode* $\widehat{u}$ *obtained by comparing Grid 1–Grid 4 with the most refined grid (Grid 5). The grid resolutions* (N_x, N_y) *are: Grid 1* (48×60)*, Grid 2* (60×72)*, Grid 3* (80×96)*, Grid 4* (96×120) *and Grid 5* (108×132)*. The Reynolds number is* $Re = 100$*, the spanwise wavenumber is* $k_z = 0.023$ *and the temporal frequency is* $\omega = 0.09$.

converging relative error compared with the most refined grid (Grid 5) as grid resolution increases at $Re = 100$, $k_z = 0.023$ and $\omega = 0.09$. We find that the relative error is below $10\,\%$ for $\widehat{u}(x, y)$, by comparing $(N_x \times N_y) = (96 \times 120)$ grid (Grid 4) results with the most refined grid of $(N_x \times N_y) = (108 \times 132)$ (Grid 5).

https://doi.org/10.1017/flo.2026.10055 Published online by Cambridge University Press

Table A1. *Computational costs of biglobal input–output analysis (run in series) for various grid resolutions associated with parameters* $\omega = 1.0$, $k_z = 0.55$ *and* $Re = 100$.

Grid ($N_x \times N_y$)	**CPU time (s)**	**Memory (GB)**
48×60	76.98	3.65
64×80	293.09	8.78
80×96	1563.45	24.23
96×120	5574.53	38.45
108×132	11643.02	86.24

Appendix B. Benchmark study of computational time and memory of input–output analysis

Table A1 compares the CPU time and memory for input–output analysis over five different grid resolutions ranging from $(N_x, N_y) = (48, 60)$ to $(N_x, N_y) = (108 \times 132)$ associated with parameters $Re = 100$, $k_z = 0.55$ and $\omega = 1$, which allows us to predict required computational resources at other grid resolutions.

References

Almeida, G. P., Durao, D. F. G., & Heitor, M. V. (1993). Wake flows behind two-dimensional model hills. *Experimental Thermal and Fluid Science*, *7*(1), 87–101.

Angot, P. (1999). Analysis of singular perturbations on the Brinkman problem for fictitious domain models of viscous flows. *Mathematical Methods in the Applied Sciences*, *22*(16), 1395–1412.

Bagheri, S., Henningson, D., Hœpffner, J., & Schmid, P. J. (2009). Input–output analysis and control design applied to a linear model of spatially developing flows. *Applied Mechanics Reviews*, *62*(2), 1–27.

Bamieh, B., & Dahleh, M. (2001). Energy amplification in channel flows with stochastic excitation. *Physics of Fluids*, *13*(11), 3258–3269.

Belcher, S. E., & Hunt, J. C. R. (1998). Turbulent flow over hills and waves. *Annual Review of Fluid Mechanics*, *30*(1), 507–538.

Brandt, L. (2014). The lift-up effect: The linear mechanism behind transition and turbulence in shear flows. *European Journal of Mechanics-B/Fluids*, *47*, 80–96.

Breuer, M., Peller, N., Rapp, C., & Manhart, M. (2009). Flow over periodic hills–numerical and experimental study in a wide range of Reynolds numbers. *Computers & Fluids*, *38*(2), 433–457.

Brunton, S. L., & Noack, B. R. (2015). Closed-loop turbulence control: Progress and challenges. *Applied Mechanics Reviews*, *67*(5), 050801.

Burns, K. J., Vasil, G. M., Oishi, J. S., Lecoanet, D., & Brown, B. P. (2020). Dedalus: A flexible framework for numerical simulations with spectral methods. *Physical Review Research*, *2*(2), 023068.

Carbou, G., & Fabrie, P. (2003). Boundary layer for a penalization method for viscous incompressible flow. *Advances in Differential Equations*, *8*(12), 1453–1480.

Chavarin, A., Gomez-de Segura, G., Garcia-Mayoral, R., & Luhar, M. (2021). Resolvent-based predictions for turbulent flow over anisotropic permeable substrates. *Journal of Fluid Mechanics*, *913*, A24.

Chavarin, A., & Luhar, M. (2020). Resolvent analysis for turbulent channel flow with riblets. *AIAA Journal*, *58*(2), 589–599.

de Vicente, J., Basley, J., Meseguer-Garrido, F., Soria, J., & Theofilis, V. (2014). Three-dimensional instabilities over a rectangular open cavity: From linear stability analysis to experimentation. *Journal of Fluid Mechanics*, *748*, 189–220.

Deville, M. O., Fischer, P. F., & Mund, E. H. (2002). *High-order methods for incompressible fluid flow*, vol. *9*. Cambridge University Press.

Diosady, L. T., & Murman, S. M. 2014, DNS of flows over periodic hills using a discontinuous Galerkin spectral-element method. In: *44th AIAA Fluid Dynamics Conference*, p. 2784.

Engels, T., Kolomenskiy, D., Schneider, K., & Sesterhenn, J. (2015). Numerical simulation of fluid–structure interaction with the volume penalization method. *Journal of Computational Physics*, *281*, 96–115.

Farrell, B. F., & Ioannou, P. J. (1993). Stochastic forcing of the linearized Navier–Stokes equations. *Physics of Fluids A: Fluid Dynamics*, *5*(11), 2600–2609.

Feng, D., Gupta, V., Li, L. K. B., & Wan, M. (2024). Resolvent analysis for predicting energetic structures in the far wake of a wind turbine. *Physics of Fluids*, *36*(8), 085101.

Fischer, P., Lottes, J., & Tufo, H. (2007). *Nek5000*. Technical report, Argonne National Laboratory (ANL).

Flynn, Z., Bae, H. J., & Goza, A. (2024). Towards an immersed-boundary resolvent analysis framework for wall-bounded flows with various surface configurations. In *AIAA Aviation Forum and Ascend 2024* (p. 3870).

https://doi.org/10.1017/flo.2026.10055 Published online by Cambridge University Press

Frank-Shapir, O., & Gluzman, I. (2025). Choosing between active and passive flow control via input–output analysis: Application to Couette flow. *IEEE Control Systems Letters*, *9*, 715–720.

Fukami, K., & Araki, R. (2026). Information-theoretic machine learning for time-varying mode decomposition of separated aerodynamic flows. *AIAA Journal*, *64*(2), 605–613.

Gross, A., Marks, C., & Sondergaard, R. (2024). Laminar separation control for Eppler 387 airfoil based on resolvent analysis. *AIAA Journal*, *62*(4), 1487–1502.

Günther, A., & Von Rohr, P. R. (2003). Large-scale structures in a developed flow over a wavy wall. *Journal of Fluid Mechanics*, *478*, 257–285.

Hester, E. W., Vasil, G. M., & Burns, K. J. (2021). Improving accuracy of volume penalised fluid-solid interactions. *Journal of Computational Physics*, *430*, 110043.

Ho, C.-M., & Huerre, P. (1984). Perturbed free shear layers. *Annual Review of Fluid Mechanics*, *16*, 365–424.

Hou, W., & Colonius, T. (2023). Three-dimensional stability and resolvent analysis of external flows over spanwise-homogeneous immersed bodies. In *AIAA AVIATION 2023 Forum* (p. 3414).

Houtman, J., Timme, S., & Sharma, A. (2023). Resolvent analysis of a finite wing in transonic flow. *Flow*, *3*, E14.

Hwang, Y., & Cossu, C. (2010). Linear non-normal energy amplification of harmonic and stochastic forcing in the turbulent channel flow. *Journal of Fluid Mechanics*, *664*, 51–73.

Islam, M. R., & Sun, Y. (2024). Identification of cross-frequency interactions in compressible cavity flow using harmonic resolvent analysis. *Journal of Fluid Mechanics*, *1000*, A13.

Jin, B., Symon, S., & Illingworth, S. J. (2021). Energy transfer mechanisms and resolvent analysis in the cylinder wake. *Physical Review Fluids*, *6*(2), 024702.

Jouin, A., Robinet, J. C., & Cherubini, S. (2024). Stability of the flow over superhydrophobic micro roughnesses: The influence of the interface. *International Journal of Thermofluids*, *23*, 100707.

Jovanović, M. R. (2021). From bypass transition to flow control and data-driven turbulence modeling: An input–output viewpoint. *Annual Review of Fluid Mechanics*, *53*(1), 311–345.

Jovanović, M. R., & Bamieh, B. (2005). Componentwise energy amplification in channel flows. *Journal of Fluid Mechanics*, *534*, 145–183.

Julien, K., & Watson, M. (2009). Efficient multi-dimensional solution of PDEs using Chebyshev spectral methods. *Journal of Computational Physics*, *228*(5), 1480–1503.

Kotapati, R. B., Mittal, R., Marxen, O., Ham, F., You, D., & Cattafesta, L. N., III (2010). Nonlinear dynamics and synthetic-jet-based control of a canonical separated flow. *Journal of Fluid Mechanics*, *654*, 65–97.

Kutz, J. N., Brunton, S. L., Brunton, B. W., & Proctor, J. L. (2016). *Dynamic mode decomposition: Data-driven modeling of complex systems*. SIAM.

Li, Z., & Yang, X. (2024). Resolvent-based motion-to-wake modelling of wind turbine wakes under dynamic rotor motion. *Journal of Fluid Mechanics*, *980*, A48.

Li, S., Zhou, Z., Yang, X., He, G., & Chen, H. (2025). Flow statistics and similarity in rough-wall periodic hill flows. *Physical Review Fluids*, *10*(10), 104608.

Lin, C.-T., Tsai, M.-L., & Tsai, H.-C. (2023). Flow control of a plunging cylinder based on resolvent analysis. *Journal of Fluid Mechanics*, *967*, A41.

Liu, Q., & Gaitonde, D. (2021). Acoustic response of turbulent cavity flow using resolvent analysis. *Physics of Fluids*, *33*(5), 056102.

Liu, C., & Gayme, D. F. (2020). An input–output based analysis of convective velocity in turbulent channels. *Journal of Fluid Mechanics*, *888*, A32.

Liu, C., & Gayme, D. F. (2021). Structured input–output analysis of transitional wall-bounded flows. *Journal of Fluid Mechanics*, *927*, A25.

Liu, C., Gluzman, I., Lozier, M., Midya, S., Gordeyev, S., Thomas, F. O., & Gayme, D. F. (2022). Spatial input–output analysis of actuated turbulent boundary layers. *AIAA Journal*, *60*(11), 6313–6327.

Liu, Q., Sun, Y., Yeh, C.-A., Ukeiley, L. S., Cattafesta, L. N., III, & Taira, K. (2021). Unsteady control of supersonic turbulent cavity flow based on resolvent analysis. *Journal of Fluid Mechanics*, *925*, A5.

Luhar, M., Sharma, A. S., & McKeon, B. J. (2015). A framework for studying the effect of compliant surfaces on wall turbulence. *Journal of Fluid Mechanics*, *768*, 415–441.

McKeon, B. J. (2017). The engine behind (wall) turbulence: Perspectives on scale interactions. *Journal of Fluid Mechanics*, *817*, P1.

Mittal, R., & Iaccarino, G. (2005). Immersed boundary methods. *Annual Review of Fluid Mechanics*, *37*(1), 239–261.

Moarref, R., & Jovanović, M. R. (2010). Controlling the onset of turbulence by streamwise travelling waves. Part 1. Receptivity analysis. *Journal of Fluid Mechanics*, *663*, 70–99.

Moarref, R., & Jovanović, M. R. (2012). Model-based design of transverse wall oscillations for turbulent drag reduction. *Journal of Fluid Mechanics*, *707*, 205–240.

Moradi, H. V., & Floryan, J. M. (2014). Stability of flow in a channel with longitudinal grooves. *Journal of Fluid Mechanics*, *757*, 613–648.

Naseri, M., & Zare, A. (2025). Turbulence modeling over riblets via domain transformation. arXiv preprint arXiv: 2501.03542.

https://doi.org/10.1017/flo.2026.10055 Published online by Cambridge University Press

Patera, A. T. (1984). A spectral element method for fluid dynamics: Laminar flow in a channel expansion. *Journal of Computational Physics*, *54*(3), 468–488.
Peskin, C. S. (2002). The immersed boundary method. *Acta Numerica*, *11*, 479–517.
Picella, F., Loiseau, J.-C., Lusseyran, F., Robinet, J.-C., Cherubini, S., & Pastur, L. (2018). Successive bifurcations in a fully three-dimensional open cavity flow. *Journal of Fluid Mechanics*, *844*, 855–877.
Ran, W., Zare, A., & Jovanović, M. R. (2021). Model-based design of riblets for turbulent drag reduction. *Journal of Fluid Mechanics*, *906*, A7.
Rapp, C., & Manhart, M. (2011). Flow over periodic hills: An experimental study. *Experiments in Fluids*, *51*(1), 247–269.
Ribeiro, J. H. M., & Taira, K. (2024). Triglobal resolvent-analysis-based control of separated flows around low-aspect-ratio wings. *Journal of Fluid Mechanics*, *995*, A13.
Rolandi, L. V., Ribeiro, J. H. M., Yeh, C.-A., & Taira, K. (2024). An invitation to resolvent analysis. *Theoretical and Computational Fluid Dynamics*, *38*(5), 603–639.
Rolandi, L. V., Smith, L., Amitay, M., Theofilis, V., & Taira, K. (2025). Biglobal resolvent analysis of separated flow over a NACA0012 airfoil. *Journal of Fluid Mechanics*, *1021*, A53.
Rossiter, J. E. (1964). Wind-tunnel experiments on the flow over rectangular cavities at subsonic and transonic speeds. *Aeronautical Research Council Reports and Memoranda*, *3438*.
Rowley, C. W., & Dawson, S. T. M. (2017). Model reduction for flow analysis and control. *Annual Review of Fluid Mechanics*, *49*(1), 387–417.
Schmid, P. J. (2010). Dynamic mode decomposition of numerical and experimental data. *Journal of Fluid Mechanics*, *656*, 5–28.
Schmid, P. J., & Henningson, D. S. (2012). *Stability and transition in shear flows*, vol. *142*. Springer Science & Business Media.
Sun, Y., Liu, Q., Cattafesta, L. N., III, Ukeiley, L. S., & Taira, K. (2020). Resolvent analysis of compressible laminar and turbulent cavity flows. *AIAA Journal*, *58*(3), 1046–1055.
Sun, Y., Taira, K., Cattafesta, L. N., III, & Ukeiley, L. S. (2017). Biglobal instabilities of compressible open-cavity flows. *Journal of Fluid Mechanics*, *826*, 270–301.
Szumbarski, J., & Floryan, J. (2006). Transient disturbance growth in a corrugated channel. *Journal of Fluid Mechanics*, *568*, 243–272.
Taira, K., Brunton, S. L., Dawson, S. T., Rowley, C. W., Colonius, T., McKeon, B. J., Schmidt, O. T., Gordeyev, S., Theofilis, V., & Ukeiley, L. S. (2017). Modal analysis of fluid flows: An overview. *AIAA Journal*, *55*(12), 4013–4041.
Taira, K., & Colonius, T. (2007). The immersed boundary method: A projection approach. *Journal of Computational Physics*, *225*(2), 2118–2137.
Taira, K., Hemati, M. S., Brunton, S. L., Sun, Y., Duraisamy, K., Bagheri, S., Dawson, S. T., & Yeh, C.-A. (2020). Modal analysis of fluid flows: Applications and outlook. *AIAA Journal*, *58*(3), 998–1022.
Tatsumi, T., & Yoshimura, T. (1990). Stability of the laminar flow in a rectangular duct. *Journal of Fluid Mechanics*, *212*, 437–449.
Theofilis, V. (2011). Global linear instability. *Annual Review of Fluid Mechanics*, *43*(1), 319–352.
Thomareis, N., & Papadakis, G. (2018). Resolvent analysis of separated and attached flows around an airfoil at transitional Reynolds number. *Physical Review Fluids*, *3*(7), 073901.
Trefethen, L. N. (2000). *Spectral methods in MATLAB*. SIAM.
Trefethen, L. N., Trefethen, A. E., Reddy, S. C., & Driscoll, T. A. (1993). Hydrodynamic stability without eigenvalues. *Science*, *261*(5121), 578–584.
Verzicco, R. (2023). Immersed boundary methods: Historical perspective and future outlook. *Annual Review of Fluid Mechanics*, *55*(1), 129–155.
Weideman, J. A., & Reddy, S. C. (2000). A MATLAB differentiation matrix suite. *ACM Transactions on Mathematical Software (TOMS)*, *26*(4), 465–519.
Wheeler, A. P. S., & Sandberg, R. D. (2016). Numerical investigation of the flow over a model transonic turbine blade tip. *Journal of Fluid Mechanics*, *803*, 119–143.
Xiao, H., Wu, J.-L., Laizet, S., & Duan, L. (2020). Flows over periodic hills of parameterized geometries: A dataset for data-driven turbulence modeling from direct simulations. *Computers & Fluids*, *200*, 104431.
Yeh, C.-A., Benton, S. I., Taira, K., & Garmann, D. J. (2020). Resolvent analysis of an airfoil laminar separation bubble at Re = 500 000. *Physical Review Fluids*, *5*(8), 083906.
Yeh, C.-A., & Taira, K. (2019). Resolvent-analysis-based design of airfoil separation control. *Journal of Fluid Mechanics*, *867*, 572–610.
Yu, K. H., Teo, C. J., & Khoo, B. C. (2016). Linear stability of pressure-driven flow over longitudinal superhydrophobic grooves. *Physics of Fluids*, *28*(2), 022001.
Zhou, Z., Yang, X. I. A., Zhang, F., & Yang, X. (2023). A wall model learned from the periodic hill data and the law of the wall. *Physics of Fluids*, *35*(5), 055108.

Cite this article: George J. and Liu C. (2026). Biglobal input–output analysis of separated flow over a periodic hill. *Flow*, *6*, E17. https://doi.org/10.1017/flo.2026.10055

https://doi.org/10.1017/flo.2026.10055 Published online by Cambridge University Press